POLITECNICO
MILANO 1863

SCUOLA DI INGEGNERIA INDUSTRIALE
E DELL'INFORMAZIONE

# Method Development for Poisson's Ratio Determination in Cartilage Using Fibril-Reinforced Models

Tesi di Laurea Magistrale in
Biomedical Engineering - Ingegneria Biomedica

Author: **Marco Sartorio**

Student ID: 233657
Advisors: Viktor Jönsson, Prof. Hanna Isaksson, Prof. Emiliano Votta
Academic Year: 2024-2025

# Abstract

Articular cartilage (AC) is a highly anisotropic soft tissue whose mechanical behavior arises from the interaction between the collagen network, proteoglycan matrix, and interstitial fluid. Accurate identification of its intrinsic material properties is essential for developing predictive computational models of knee joint. This thesis presents a method to estimate Poisson ratio in AC using a fibril-reinforced poroelastic (FRPE) material model. The study is based on previously performed unconfined compression stress-relaxation experiments on cylindrical bovine knee AC samples, combined with time-resolved synchrotron-based-X-ray phase-contrast micro-computed tomography (SR-PhC-microCT) scans acquired during the loading protocol. Reaction forces were extracted from the mechanical data, while a dedicated image-based workflow was developed to compute areal strains at incremental compressive strains. Two idealized cylindrical finite element models and one sample-specific finite element model were developed to simulate the experimental test. A novel optimization framework was implemented to simultaneously fit axial and transverse responses for material parameter identification. The approach resulted in a set of parameters that enabled the idealized model of the first sample to successfully reproduce its overall mechanical behavior, demonstrating the potential of the method for parameter estimation. In contrast, for the second sample, the models were unable to match both axial force and lateral expansion at the same time, likely due to the inability of the adopted constitutive model to faithfully reproduce the sample-specific mechanical behavior. The inclusion of the transverse response revealed additional inter-sample mechanical variability that is not accounted for when fitting axial force alone, as commonly done in previous studies.

# Abstract in lingua italiana

La cartilagine articolare (AC) è un tessuto molle altamente anisotropo, il cui comportamento meccanico deriva dall'interazione tra la rete di collagene, la matrice di proteoglicani e il fluido interstiziale. La corretta identificazione delle proprietà meccaniche intrinseche della cartilagine è fondamentale per lo sviluppo di modelli computazionali predittivi dell'articolazione del ginocchio. In questa tesi viene proposto un metodo per stimare il coefficiente di Poisson della cartilagine articolare utilizzando un modello di materiale poroelastico fibrorinforzato (FRPE). Lo studio si basa su prove di compressione non confinata con rilassamento dello sforzo, eseguite in precedenza su campioni cilindrici di cartilagine articolare bovina, in combinazione con scansioni microtomografiche a contrasto di fase ai raggi X basate su sincrotrone (SR-PhC-microCT), acquisite in tempo reale durante il protocollo di carico. Dai dati meccanici sono state ricavate le forze di reazione, mentre è stata sviluppata una procedura di elaborazione delle immagini per calcolare la deformazione areale ad incrementi successivi di compressione. Sono stati sviluppati due modelli agli elementi finiti di geometria cilindrica idealizzata e un modello agli elementi finiti campione-specifico per simulare il protocollo sperimentale. È stata implementata una procedura di ottimizzazione che consente di calibrare simultaneamente i comportamenti assiale e trasversale, al fine di ottenere una stima più accurata dei parametri del modello di materiale. L'approccio ha portato all'identificazione di un insieme di parametri che ha consentito al modello idealizzato del primo campione di riprodurre fedelmente il suo comportamento meccanico complessivo, dimostrando la validità e il potenziale del metodo per la stima dei parametri del materiale. Nel caso del secondo campione, tuttavia, i modelli non sono riusciti a rappresentare contemporaneamente la forza assiale e l'espansione laterale, probabilmente a causa di peculiarità meccaniche specifiche del campione non completamente descritte dall'attuale formulazione del modello costitutivo. L'inclusione della risposta trasversale ha inoltre evidenziato una maggiore variabilità meccanica inter-campione, non rilevabile quando l'analisi è condotta sulla sola forza assiale, come comunemente riportato in studi precedenti.

# Contents

**Abstract** **1**

**Abstract in lingua italiana** **2**

**Contents** **3**

**1 Introduction** **5**
1.1 State-of-the-Art . . . 6
1.2 Aim . . . 7

**2 Knee joint** **8**

**3 Structure and composition of articular cartilage** **10**
3.1 Collagen . . . 12
3.2 Interstitial fluid . . . 12
3.3 Proteoglycans . . . 12
3.4 Articular cartilage degeneration . . . 13

**4 Articular cartilage biomechanics** **14**
4.1 Viscoelastic properties . . . 15
4.2 Nonlinear behavior . . . 18
4.3 Characterization . . . 18
4.3.1 Unconfined compression . . . 18

**5 Computational modeling of articular cartilage** **20**
5.1 Non-fibrillar matrix . . . 20
5.2 Fibrillar matrix . . . 21
5.3 Interstitial fluid . . . 23

**6 Materials and methods** **25**
6.1 Experimental data . . . 26
6.2 Image data . . . 27
6.3 Idealized FE model . . . 32

6.4 Material properties . . . . . 34
6.5 Sample-specific model . . . . . 37

**7 Results** **39**
7.1 Experimental areal strain evaluation . . . . . 39
7.2 Constitutive paramer identification through the idealized finite element model . . 39
7.3 Fitting of the sample-specific model: sample 02 . . . . . 41

**8 Discussion** **44**
8.1 Interpretation of the mechanical response . . . . . 44
8.2 Limitations . . . . . 47

**9 Conclusions** **48**

**Bibliography** **49**

**A List of Figures** **57**

**B List of Tables** **60**

**Acknowledgements** **61**

# 1 Introduction

Walking, climbing stairs, sitting to standing, and running are fundamental daily motions that rely heavily on the knee joint—the largest lower limb motor joint—making its overall health essential in maintaining an adequate quality of life. Conditions such as overweight or joint disorders are associated with non-physiological stress distributions that can lead to the development of knee osteoarthritis (OA). OA is the most common pathology affecting the knee joint, resulting in severe damage to the whole joint, including progressive loss of articular cartilage (AC).

The economic impact of OA is considerable, accounting for an estimated 1-2.5% of the gross domestic product (GDP) of Western countries [1]. In Europe, more than 100 million individuals are affected [2] and the progressive aging of the world population is making OA not only a significant burden on health care systems, but also a major threat to quality of life [3]. Prevention would be the most desirable and cost-effective strategy, but it is currently only partially feasible due to the lack of early diagnostic tools and the limited number of randomized trials showing effectiveness of primary prevention [4]. Currently, preventive efforts are mostly restricted to addressing modifiable risk factors such as obesity and prior knee injuries [5].

Furthermore, the disease often progresses gradually until reaching a stage where total knee arthroplastly (TKA) becomes the only viable treatment [6]. Forecasts indicate that the demand for TKA in the United States will increase by approximately 221% from 2020 to 2040 [7].

This dramatic increase highlights the urgent need for effective strategies aimed at early diagnosis and disease-modifying interventions. In this context, several surgical options have been developed, including bone marrow stimulation techniques (e.g. microfracture, drilling, abrasion), osteochondral grafts (autografts and allografts), and autologous chondrocyte implantation [8]. Tissue engineering and regenerative medicine offer promising strategies for OA treatment by aiming to repair damaged cartilage. The limited regenerative ability of AC to heal chondral defects has prompted growing interest in new treatment alternatives such as hydrogels loaded with chondrocytes and mesenchymal stem cells (MSCs) [8–10]. While these approaches show potential, they are still constrained by variable outcomes, high costs, risk of fibrocartilage formation, and the need of multiple surgeries [8–10]. Emerging strategies under investigation include paracrine activity stimulation, magnetically delivery systems, and MSC-derived exosomes [8].

Although biological treatments hold great promise in cartilage repair, their translation into

clinical practice is still limited by issues of safety, efficacy, and long-term functionality [8, 10]. To address these challenges, the integration of imaging techniques with computational modeling has emerged as a powerful strategy to support diagnosis, design patient-specific treatments, and predict the progression of diseases and therapeutic outcomes [11].

In biomechanics, the finite element method (FEM) is commonly used to create models of anatomical structures, offering the opportunity to perform a comprehensive analysis of their response under various physiological or pathological conditions. This approach allows quantifying biomechanical information that would be difficult or impossible to detect experimentally, including stress distribution or and localized strains [11]. Patient-specific modeling of the knee joint based on the FEM offers a promising tool for predicting disease progression and designing personalized treatments. The first model of this kind was developed by Mononen et al., who integrated the use of MRI to reconstruct the patient-specific geometry of AC, of FEM to quantify AC biomechanics, and an analytical model of AC degeneration to predict the patient-specific progression of OA [2]. Focusing on cumulative mechanical overloading on the AC collagen fibrils network, the model was validated using 4-year follow-up of the medial tibiofemoral compartment [2].

To obtain accurate results, FEM models must include constitutive models that reflect the mechanical response of the specific material [8]. The constitutive parameters of such models should be identified by fitting the relevant constitutive model to the stress-strain data yielded by experimental mechanical tests, which should be designed to isolate the effects of single constitutive parameters. However, the complexity of AC geometry and microstructure, and the resulting heterogeneous and anisotropic stress-strain behavior of AC tissue do not allow for such approach [12]. A common alternative strategy is to adopt an inverse modeling approach, where the simulation reproduces the experimental setup and the unknown parameters are then estimated iteratively by minimizing the discrepancy between the computational results and the corresponding experimental data.

## 1.1. State-of-the-Art

Although inverse modeling approaches are widely adopted for the identification of AC constitutive parameters, most studies have primarily focused on parameters governing the overall stiffness and permeability of the tissue [13–15]. From a mechanical perspective, AC is commonly described as a biphasic material consisting of a solid and a fluid phase [16]. In a constitutive formulation commonly adopted for the computational description of AC [13–15], the solid phase is typically decomposed into a fibrillar component, representing the collagen network, and a non-fibrillar component, representing the proteoglycan-rich matrix. Within these formulations, the non-fibrillar Poisson's ratio represents a material parameter governing the deformation behavior of the solid matrix. In AC experimental studies, Poisson's ratio is commonly estimated from unconfined compression tests through optical measurements of axial and lateral strains [17, 18]. However, the resulting values correspond to an apparent Poisson's ratio that reflects the overall

macroscopic response of the tissue under specific loading conditions. Consequently, this apparent value cannot be directly used to describe the non-fibrillar matrix within fibril-reinforced constitutive models. Despite its explicit presence in these formulations, non-fibrillar Poisson's ratio has not been systematically investigated in the literature. To date, one study attempted to relate experimentally measured apparent Poisson's ratios to the intrinsic non-fibrillar values through simplifying assumptions, including prescribed linear relationships between the two values [14]. However, the proposed relationship was based on previously assumed non-fibrillar Poisson's ratio values [13], rather than derived through an independent identification procedure. Since the non-fibrillar matrix governs the equilibrium response of AC, assumptions regarding its Poisson's ratio may lead to inaccurate predictions of the overall mechanical behavior of the tissue.

Moreover, OA progression is known to induce significant changes in collagen architecture, proteoglycan content, and water distribution within the tissue [15, 19–21]. These modifications have been widely linked to variations in mechanical properties such as stiffness, permeability, and overall load-bearing capacity [15, 19–21]. Conversely, the literature addressing Poisson's ratio in osteoarthritic cartilage remains limited. Predictive knee joint models for OA currently assume a constant Poisson's ratio, while other mechanical properties change in the models [2]. However, its mechanical implications have not been systematically assessed. Therefore, the development of a method for non-fibrillar Poisson's ratio determination in AC is crucial for further improvements of the reliability and predictive capability of patient-specific knee joint models.

## 1.2. Aim

The aim of this thesis is the development of a method for non-fibrillar Poisson ratio determination in knee articular cartilage for a fiber-reinforced material model using finite element analysis. The analysis is based on synchrotron imaging and mechanical data of bovine AC samples acquired by Dejea et al. [22]. These experimental datasets were used to create two idealized and one sample-specific FE model of AC. A parameter fitting procedure, based on the experimental data, was performed to identify the material model parameters, including Poisson ratio.

# 2 | Knee joint

The knee represents the largest and most loaded joint within the human body, playing an important role in locomotion. Its main functions include to allow almost frictionless flexion-extension, absorb functional loads, and provide stability [23].

While flexion-extension is the primary movement of the joint and occurs in the sagittal plane, internal and external rotations in the transverse plane are also possible [24]. From the structural standpoint, the knee includes both the tibiofemoral and patellofemoral joints [24]. The tibiofemoral joint connects the convex femoral condyles and the relatively flat tibial plateau, while the patellofemoral joint involves the articulation between the patella and the throclear groove of the femur [25] (Figure 2.1).

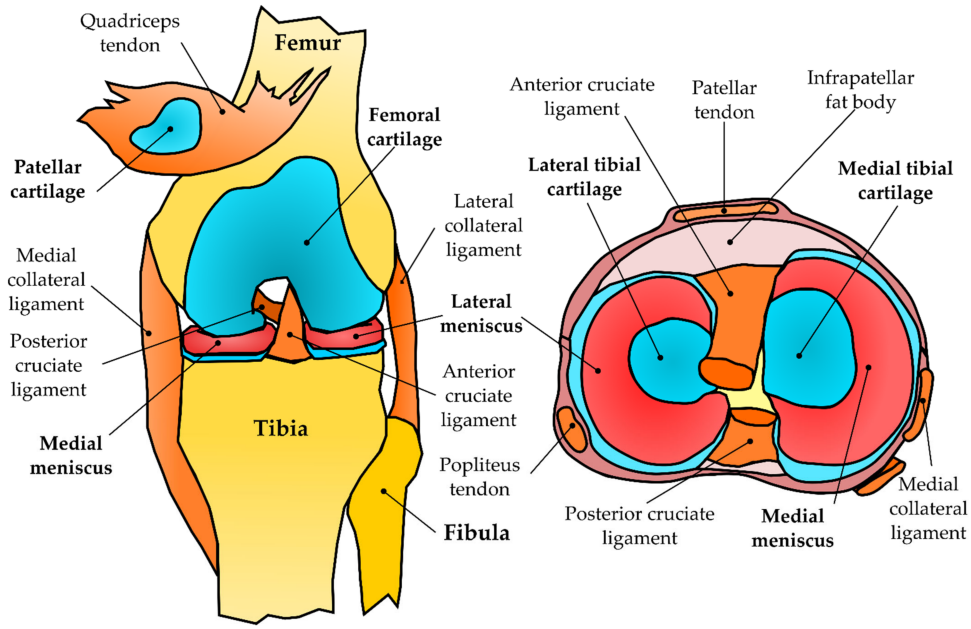


Figure 2.1: Schematic of the knee joint anatomy, frontal (left) and coronal (right) views [26].

The joint surfaces are subjected to both compressive and shear loads, and their ability to withstand such loading conditions is related to the presence of several soft tissues [27]. The articular surfaces are covered by a film of hyaline articular cartilage, which plays a crucial role in reducing friction and allowing for smooth interaction between the articulating bone surfaces [28]. The menisci are fibrocartilaginous components located on the surface of the tibial plateau capable

of enlarging the tibiofemoral contact area, thereby reducing contact pressures [29]. Owing to their high deformability, menisci withstand more than half of the body weight during dynamic movements and are therefore regarded as the main shock absorber within the whole joint [30]. Ligaments act as passive stabilizers that generate tension in response to external forces or joint movements, and help redistribute loads throughout the knee to maintain stability in all planes [23]. The joint capsule contributes to stability by constraining the whole knee joint and limiting non-physiological motions, as it is connected to muscles and ligaments [31]. The internal synovial fluid is fundamental for the lubrication of the articular surfaces and the nourishment of avascular components such as menisci and cartilage [31] (Figure 2.1).

The most common musculoskeletal knee disorders include knee osteoarthritis (OA), knee ligament injury, and meniscus injury [32]. Among these, knee OA is the most prevalent condition, affecting approximately 22.9% of individuals aged 40 years and older worldwide [33]. These pathologies are typically associated with reduced knee flexion angle and muscles contractile capacity, slower gait, and increased articular contact pressures [32]. However, our ability to fully understand and quantify these effects faces limitations such as excessive simplification of anatomical and mechanical properties in computational models, and restrictions on the analyzed motions, often leading to inconsistent results [32]. Both the physiological and pathological knee biomechanics needs to be further studied, together with the development of more realistic and reliable computational models, in order to better support clinical practice and the design of assistive devices.

# 3 | Structure and composition of articular cartilage

Articular cartilage (AC) is an avascular, aneural, multilayered connective tissue covering the surface of the bones in a joint. Its thickness is sex-, site-, and BMI-specific, generally ranging from 1-3 mm in the human knee. Within the knee joint, the patellar cartilage is typically the thickest, particularly in females [28, 34]. AC composition and thickness vary among different anatomical sites as an adaptation to distinct mechanical loading conditions [34, 35], such as shear stresses in the patellar region, compressive stresses in the tibial plateau, and a combination of the two in the femoral cartilage [27].

AC tissue is primarily composed of water, collagen fibrils, chondrocytes, proteoglycans, mineral components, and matrix protein [28] (Table 3.1).

| **Component** | **Amount (%)** |
|---|---|
| Water | 70–80% |
| Collagen | 12–14% |
| Type II | 90–95% of collagen |
| Type IX | 1–5% of collagen |
| Type XI | 2–5% of collagen |
| Chondrocytes | 1–10% |
| Proteoglycans | 7–9% |
| Mineralic materials | <4% |
| Matrix proteins | <1% |

Table 3.1: General composition of AC expressed as percentage of total wet weight [28].

As AC has no blood supply, interstitial fluid diffusion plays a key role in chondrocytes nourishment and catabolites removal, making these cells metabolically active [36]. The lack of vascularization and innervation impairs the tissue's ability to heal and regenerate [36].

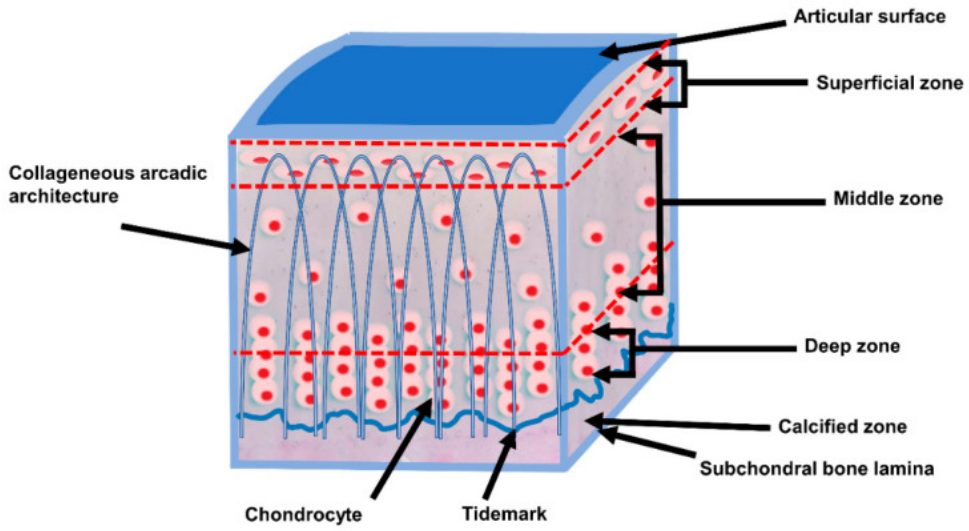


Figure 3.1: AC layers: superficial, middle, deep, and calcified zone. The image illustrates collagen fibril orientation, chondrocyte morphology, and the tidemark. Adapted from [28].

The architecture of AC displays a depth-dependent structural organization (Figure 3.1). The superficial (tangential) zone is directly in contact with the synovial fluid, and accounts for 10-20% of the total thickness of the tissue [28]. It is characterized by densely packed collagen fibrils aligned parallel to the articular surface, high water content, and flattened chondrocytes organized tangentially [28]. Proteoglycans concentration is at its lowest here [19]. The tangential layer plays a key role in shielding the deeper cartilage from shear stresses [37].

The middle (transitional) zone accounts for 40-60% of the whole tissue volume, and it contains thicker, randomly arranged collagen fibrils and a lower density of spherical chondrocytes [38]. The middle zone works as the first line of defense against compressive loads [39].

The deep (radial) zone makes up 30% of the tissue volume [28]. It is characterized by the thickest collagen fibrils, which are arranged perpendicularly to the articular surface, high proteoglycans content, low water content, and elongated chondrocytes are aligned in columnar arrays [28, 38]. The arcade-like arrangement of collagen fibrils in this zone confers the greatest resistance to compressive forces [19], [39].

The calcified zone represents a thin mineralized layer interposed between the deep non-calcified cartilage and the subchondral bone [20, 28]. This region contains sparse and hypertrophic chondrocytes; its main function consists in preventing the detachment of the collagen fibrils from the underlying bone, thereby ensuring a consistent stability against shear stresses [20] [28].

At the interface between the deep zone and the calcified cartilage lies the tidemark, a line visible in histological sections [40, 41]. The tidemark is considered the mineralization front of cartilage, and its multiplication is regarded as an early sign of OA, as it is associated with calcification advancement into the deep cartilage layer [40, 41].

In the next subsections, each constituent of CA extracellular matrix is briefly described.

## 3.1. Collagen

Collagen is the most abundant protein within the human body [42]. Collagen molecules self-assemble into fibrils, which further organize into fibers [15]. Intermolecular and intramolecular links within this structure allow for the formation of a resilient collagen network [15].

In the AC, collagen fibrils are mostly made of type II collagen, which is cross-linked with type IX and type XI collagen fibrils, leading to increased matrix integrity [28, 43]. In addition, minor quantities of other collagen types are present, contributing to the maintenance of the pericellular environment and thus supporting the integrity of chondrocytes [43].

Historically, the arcade-like and depth-dependent pattern of collagen fibrils has been described as the Benninghoff arcade structure [19, 28, 44]. This arrangement prevents excessive swelling, increases resistance to shear and compressive loads, and enhances load distribution [45].

## 3.2. Interstitial fluid

Water makes up for 70-80% of AC wet weight [28] and acts as an active structural component [19]. By contributing to the tissue's strain rate-dependent stiffness, water enables AC to absorb impact forces and withstand prolonged loading, thereby ensuring its mechanical suitability for daily joint demands [46].

The fluid filling the interstitial space of cartilage contains several dissolved ions (Na+, K+, Ca2+, Cl-), as well as small metabolites such as glucose, lactate and oxygen [39]. These solutes are essential for maintaining osmotic balance within the extracellular matrix and play a fundamental role in the mechanical behavior of the tissue [39, 47].

## 3.3. Proteoglycans

Proteoglycans consist of a core protein that is covalently bound to glycosamminoglicans (GAGs), which are negatively charged polysaccharide chains [15]. The most abundant proteoglycan within the AC is aggrecan (Figure 3.2), which forms large supramolecular aggregates by binding non-covalently with hyaluronic acid via link proteins [15, 48, 49]. These aggregates are key components of the extracellular matrix and their presence can be used as biomarker in OA and for the evaluation of the quality of tissue repair after chondral injuries [48, 49].

Since GAGs are anionic, they create a fixed charge density that draws cations and thereby regulates the osmotic balance. The ionic environment plays a central role in tissue swelling, as the ionic concentration within the AC is higher than in the surrounding synovial fluid, generating a Donnan osmotic pressure [39, 50].

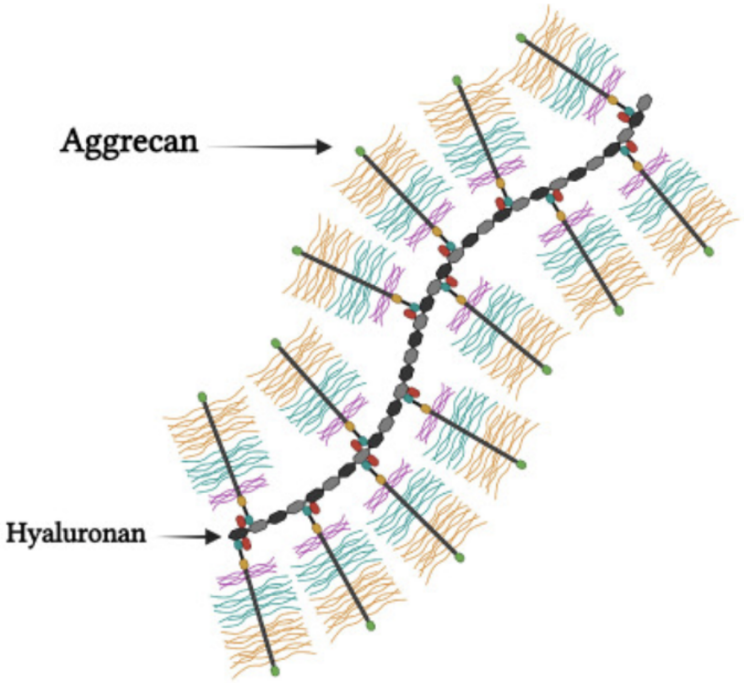


Figure 3.2: Structure of a PG aggregate: multiple aggrecan molecules bind to a central hyaluronan filament via link proteins, forming a large supramolecular complex. Adapted from [48].

## 3.4. Articular cartilage degeneration

AC degeneration, particularly in OA, results in consistent structural and biomechanical changes [15, 20]. OA can be triggered by mechanical trauma, aging, or genetic predisposition [15, 51]. Early pathological signs include disruption of the collagen network, superficial loss of PGs, tissue swelling, and abnormal chondrocyte activity [15]. As fixed charge density decreases and collagen network integrity loss progresses, the tissue's ability to counterbalance osmotic swelling is compromised, leading to further expansion and PGs loss [15]. Disease progression is associated with cartilage fissures, increased permeability, elevated water content, and reduced stiffness, eventually leading to chondrocytes death and tissue degradation [15, 19–21].

# 4 | Articular cartilage biomechanics

AC is a viscoelastic material that can be described by biphasic theory [16], as it is composed of a porous solid phase, mainly collagen fibrils and proteoglycans, and a fluid phase, primarily water containing dissolved ions and metabolites.

Darcy's law describes how a fluid flows through a porous media under the hypothesis of laminar flow conditions [19], which is typically true for a biological sample [15]. According to Darcy's law, the average fluid flux $q$ can be obtained as:

$$q = -k \nabla P \tag{4.1}$$

where $\nabla P$ is the pressure gradient, and $k$ is the hydraulic permeability, a measure of how easily the fluid can flow through a porous structure. In AC, mechanical loading induces a buildup of interstitial fluid pressure due to the low permeability of the tissue [52]. These pressure differences give rise to a gradient $\nabla P$, which is the driving force for fluid transport through the matrix [19, 28, 52].

Bovine AC $k$ ranges from $0.44 \times 10^{-15}$ $\mathrm{m^4\,N^{-1}\,s^{-1}}$ to $1.42 \times 10^{-15}$ $\mathrm{m^4\,N^{-1}\,s^{-1}}$ [47]. This hinders fluid outflow, thereby allowing for fluid pressurization and contributing to the fundamental load-bearing function of cartilage during peak loading [47]. $k$ is not homogeneous over the AC, but it decreases from the most superficial to the deepest layer [19]. Due to both differences in collagen network architecture and proteoglycans density, and the presence of the nearly impermeable boundary of the subchondral bone, fluid outflow is predominant from the superficial layer [19]. Moreover, as cartilage is compressed, the porous structure tends to compact, thereby leading to a reduction in its permeability [53].

The strain-dependent $k$ primarily influences the response of AC tissue under compressive loading, regulating the redistribution of the fluid during deformation [54]. It may play a key role in transferring loads between the ECM and the interstitial fluid in the AC [19, 54]. This load sharing mechanism may be essential in avoiding the solid components from bearing excessive compressive stress [19, 54].

The compressive Young modulus $E_c$ of bovine AC ranges between 0.24 and 0.85 MPa [47, 55], with higher values observed in the deeper regions of the tissue [47]. The compressive behavior of cartilage is primarily governed by two mechanisms: fluid pressurization, which dominates the

initial response by bearing most of the applied load, and electrostatic repulsion of negatively charged proteoglycans, which controls long-term equilibrium behavior as fixed charges are pushed closer together and interstitial fluid exudes from the solid matrix [19, 27, 28]

In contrast, the collagen network plays a key role under tensile loads, with mechanical response strongly influenced by fibrils orientation [27, 56]. In fact, the tensile Young modulus ($E_t$) is markedly higher than $E_c$, ranging from 5 to 25 MPa in bovine AC [47, 57], with the highest values observed in the surface zone [47]. This anisotropic mechanical behavior shows that collagen fibrils are highly effective in resisting tensile loading [52, 56], but tend to buckle under compression, thereby offering less resistance [58].

The Poisson ratio $\nu_s$ is an adimensional that relates the lateral expansion of a material when this is uniaxially compressed, or, conversely, the lateral contraction of the material when this is uniaxially stretched by a tensile load. For isotropic, linearly elastic, materials, $\nu_s$ is defined as:

$$\nu_s = -\frac{\epsilon_{\text{trans}}}{\epsilon_{\text{long}}} \tag{4.2}$$

where $\epsilon_{\text{trans}}$ represents the strain in the direction perpendicular to the applied load, and $\epsilon_{\text{long}}$ is the strain along the loading direction. $\nu_s$ values reported in literature for the bovine AC range between 0.1 and 0.4, mainly due to differences in the adopted experimental protocols [17, 55].

AC is anisotropic and inhomogeneous due to its highly complex nature, consisting of a fluid-saturated porous solid matrix reinforced with a depth-dependent network of collagen fibrils [55]. The local strain field within the tissue is thereby heterogeneous [59]. Collagen fibrils consistently constrain lateral expansion of AC under longitudinal compression [55]. As a result, the assumptions made to write Eq.(4.2), i.e., linear elasticity and material homogeneity, are not valid for AC. The apparent Poisson ratio measured experimentally derives from the combined mechanical response of the solid matrix — including both fibrillar (collagen) and non-fibrillar (proteoglycans) components — as well as the fluid phase [55].

The non-fibrillar Poisson ratio $\nu_m$, which is of interest in the present thesis work, characterizes the intrinsic lateral deformability of the non-fibrillar matrix in absence of fiber reinforcement. Since the total mechanical response of AC includes contributions from all its components, $\nu_m$ cannot be directly measured through conventional mechanical testing. Instead, computational modeling is required to estimate this parameter and will be discussed in Chapter 6.

## 4.1. Viscoelastic properties

Viscoelastic materials exhibit a mechanical response that is intermediate between purely elastic solids and purely viscous fluids. In an elastic solid, deformation is instantaneous and fully recoverable; in a viscous fluid, deformation is time-dependent and irreversible. Viscoelastic materials combine these two behaviors, meaning that when they are loaded part of the energy

is stored and can be recovered, while part is dissipated over time. Time dependence, strain-rate dependence, and memory effect are fundamental characteristics of such materials [60, 61].

To characterize viscoelastic behavior, creep test and stress-relaxation tests can be used. The former one consists in applying a constant stress and measuring the deformation over time, while the latter one applies a constant deformation and the stress required to maintain that deformation is monitored over time (Figure 4.1).

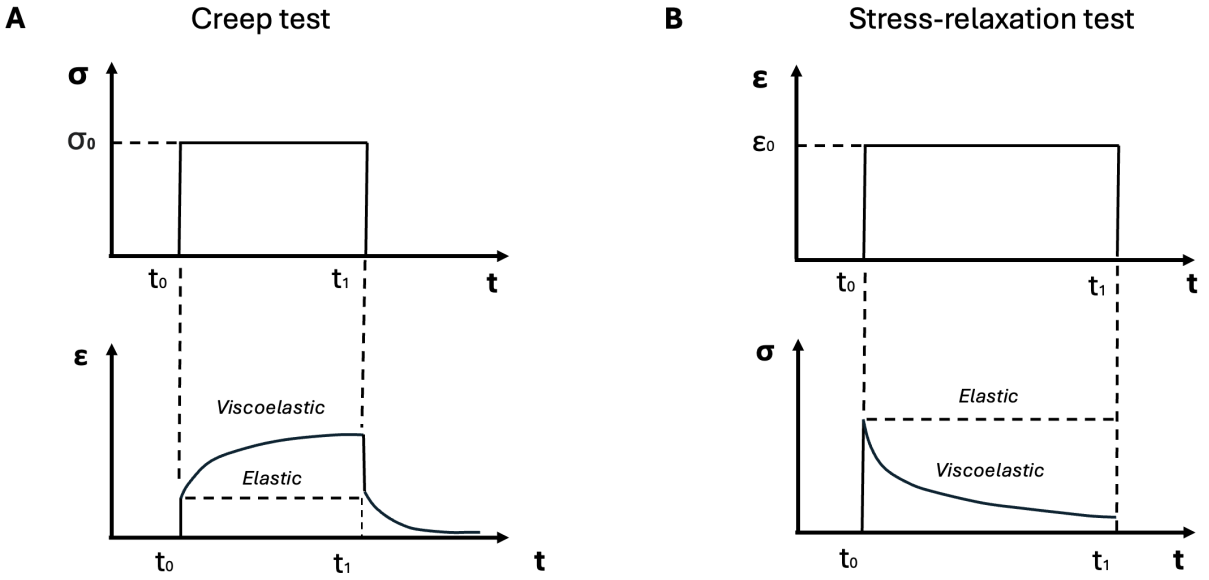


Figure 4.1: Typical mechanical responses of viscoelastic materials in a creep test and in stress-relaxation test. (A) Creep test: under the application of a constant stress, the strain shows an immediate elastic component followed by a gradual viscoelastic deformation; when the load is removed, an elastic followed by a viscoelastic recovery can be observed. (B) Stress-relaxation test: under constant strain, the initial stress decreases over time until it reaches a plateau. Adapted from [62].

These experimental responses can be quantitatively described by simple mechanical models such as Maxwell, Kelvin-Voigt, and Zener (Figure 4.2), which are commonly used to describe viscoelastic behavior [60, 61, 63, 64]. In these models, the elastic components are represented as springs following Hooke's law (Figure 4.2):

$$\sigma = E\epsilon \tag{4.3}$$

where $\sigma$ is the stress, $\epsilon$ is the strain, and $E$ is the Young's modulus. The viscous component is modeled as a dashpot governed by a Newtonian fluid law:

$$\sigma = \eta \frac{d\varepsilon}{dt} \tag{4.4}$$

where $\eta$ is the viscosity and $\frac{d\varepsilon}{dt}$ the strain rate.

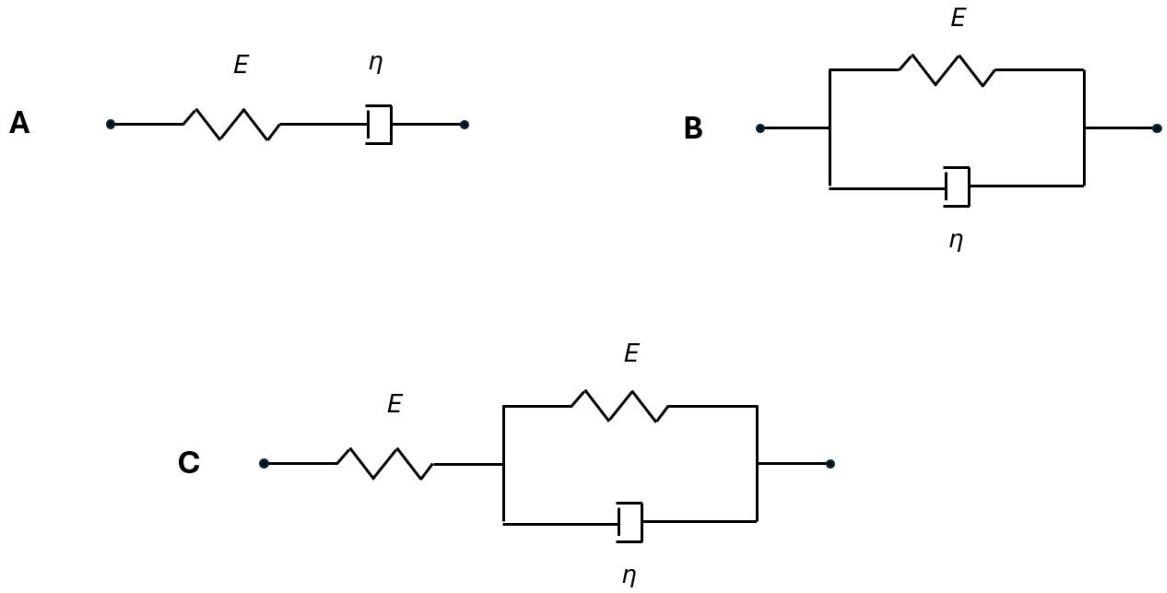


Figure 4.2: Classical mechanical models used to describe the behavior of viscoelastic materials. Maxwell model (A), Kelvin-Voigt model (B), Zener model (C) [62].

However, in biological soft tissues such as AC, viscoelasticity is more complex because it derives not only from the behavior of the solid matrix, but also from fluid-solid interactions [28]. While these models provide a simplified representation of the mechanical behavior, more advanced formulations that account for AC biphasic or triphasic nature are required [13, 65]. A detailed description of the specific material model adopted in this study is provided in Chapter 6.

As previously introduced, the AC exhibits a time-dependent mechanical behavior. Two complementary mechanisms of viscoelasticity are typically distinguished: flow-dependent and flow-independent. The flow-dependent mechanism arises from the gradual exudation of the interstitial fluid through the porous solid matrix, driven by the pressure gradients during loading. Due to high friction between the fluid and the solid phase, up to 95% of the mechanical energy is dissipated during this process [27]. The continuous loading leads the fluid to flow out of the tissue, and the contribution of its pressurization to load-bearing progressively decreases [19, 28]. Once equilibrium is reached, mechanical support is fully provided by the solid matrix [28]. The flow-independent mechanism, accounting for the remaining mechanical energy dissipation, is attributed to the intrinsic viscoelasticity of proteoglycans and collagen fibrils [27]. When the load is removed, the resulting Donnan osmotic pressure progressively drives the interstitial fluid back into cartilage layers [28].

## 4.2. Nonlinear behavior

The mechanical response of AC tissue is highly nonlinear and strongly influenced by the interaction of the fluid and solid components. When the magnitude of loading increases, the stiffness of the tissue rises progressively, a phenomenon commonly known as stress or strain hardening [47]. Collagen plays a key role in the nonlinear response of fibril-reinforced tissues, as the gradual recruitment and alignment of the fibrils under tension increases the tissue stiffness [47]. Moreover, the non-linear stiffening of the collagen network in tension affects the behavior of AC tissue under compression, as the lateral expansion is constrained [55]. During compression, the ECM undergoes structural reorganization, which alters interstitial fluid flow and contributes to a nonlinear mechanical response [47]. The compression-tension nonlinearity, along with the previously mentioned strain-dependent nonlinear permeability, are thereby essential features governing AC tissue mechanics [56, 66, 67].

## 4.3. Characterization

Depending on the anatomic site and function, a biological tissue is optimized to resist different loading conditions. While ligaments and tendons mainly withstand tensile loadings, intervertebral disks, menisci, and articular cartilage are physiologically required to withstand shear and compression [39]. As a consequence, compressive protocols are commonly used to assess AC mechanical properties. Displacement-controlled and force-controlled approaches, namely stress-relaxation and creep, can be exploited to better understand biological tissues time-dependent behavior. While the mechanical properties of proteoglycans can be mainly investigated through the study of the equilibrium phase, the collagen network properties are reflected in the peaks of the loading ramp [55]. The constraining function of collagen fibrils allows the interstitial fluid to pressurize and bear significant dynamic loads [55].

Different experimental techniques can be used to analyze AC mechanical behavior (Figure 4.3). In indentation testing, a rigid indenter compresses the cartilage surface, providing estimates of local mechanical parameters such as aggregate modulus $Ha$, $k$, and $\nu$ on small intact osteochondral samples without removing the subchondral bone [39, 47]. Conversely, in confined compression, a cylindrical cartilage specimen is loaded within an impermeable chamber through a porous platen, allowing the determination of parameters such as aggregate modulus and permeability [39, 47].

Since unconfined compression test is employed in this thesis, a dedicated section will focus on its fundamentals and experimental setup.

### 4.3.1. Unconfined compression

While confined compression test relies on restricting the fluid flow in every direction but the loading one, and indentation doesn't restrict it at all, unconfined compression allows for radial

fluid exudation (Figure 4.3).

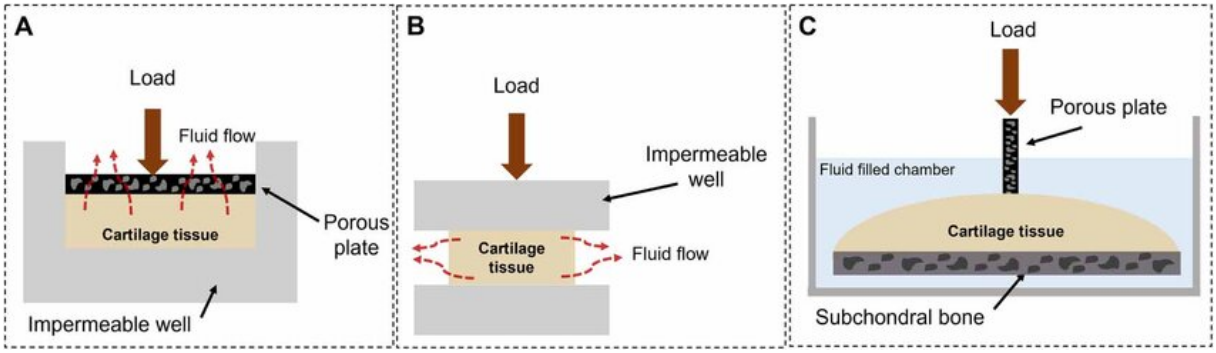


Figure 4.3: Comparative schematic of three experimental setups used to apply mechanical loading to articular cartilage - confined compression test (A), unconfined compression test (B), indentation test (C). Image taken from [27].

In unconfined compression, the cartilage sample is placed between two impervious plates. When a stress or strain is applied through the top piston, the cartilage sample is compressed longitudinally and is free to expand laterally. As the interstitial fluid is free to flow out, this configuration allows to capture the time-dependent behavior of the tissue and the osmotic effects related to ions transport. Moreover, due to its radial expansion, the multilayered anisotropic nature of AC tissue can be investigated, along with essential properties such as Poisson ratio [47].

Over the past few decades, unconfined compression testing has emerged as a method not only for characterizing native cartilage, but also for evaluating the mechanical behavior of engineered porous scaffolds, as it allows to mimic physiological conditions [68].

# 5 | Computational modeling of articular cartilage

Complex physical phenomena, such as the mechanical behavior of biological tissues, can be described by systems of differential equations. In many practical cases, however, obtaining an analytical solution is often impossible due to the complexity of the governing equations. The finite element method (FEM) addresses this challenge by approximating a problem over a discretized domain (mesh).

FEM has become an essential tool for investigating the mechanical response of soft tissues, particularly when specific parameters cannot be measured through experimental testing. Several computational approaches have been developed to capture the mechanical behavior of AC. These include poroelastic models, triphasic models, fibril-reinforced poroelastic models, viscoelastic fibril-reinforced poroelastic models and viscoelastic fibril-reinforced triphasic models [13, 16, 65, 69, 70].

Due to AC's nonlinear, anisotropic, and time-dependent response, a fibril-reinforced poroHyperelastic (FRPE) material model is adopted in this study to describe the complex mechanical behavior of the tissue. In this framework, AC is modeled as a biphasic material [16], consisting of a fluid phase and a solid phase, the latter comprising both a fibrillar matrix, representing the collagen, and a non-fibrillar matrix, representing the proteoglycans.

The total stress tensor $\boldsymbol{\sigma}_t$ reflects the combined mechanical response of the whole solid matrix and the contribution from the interstitial fluid pressure, and is formulated as follows [39]:

$$\boldsymbol{\sigma}_t = \boldsymbol{\sigma}_{\mathrm{nf}} + \boldsymbol{\sigma}_{\mathrm{f}} - P\mathbf{I} \tag{5.1}$$

where $\boldsymbol{\sigma}_{\mathrm{nf}}$ is the stress generated by the non-fibrillar matrix, $\boldsymbol{\sigma}_{\mathrm{f}}$ is the stress within the fibrillar collagen network, $P$ is the pore fluid pressure, and $\mathbf{I}$ is the second-order identity tensor.

## 5.1. Non-fibrillar matrix

The porous non-fibrillar matrix is modeled using a Neo-Hookean hyperelastic material [65]. Hooke's law can be applied for low strains only, but AC can undergo deformations up to 30%

under physiological loading [71]. Due to interstitial fluid exudation, which leads to a reduction in tissue's volume, the matrix is assumed to be compressible [15]. Furthermore, the non-linear mechanical response of the matrix is included in the constitutive model.

The corresponding Cauchy stress tensor $\sigma_{\mathrm{nf}}$ is given by [39]:

$$\boldsymbol{\sigma}_{\mathrm{nf}} = \frac{1}{2}K_{\mathrm{nf}}(J - J^{-1})\mathbf{I} + \frac{G_{\mathrm{nf}}}{J}\left(\mathbf{F}\mathbf{F}^{\mathrm{T}} - J^{2/3}\mathbf{I}\right), \tag{5.2}$$

where $K_{\mathrm{nf}}$ and $G_{\mathrm{nf}}$ are the bulk and shear moduli of the non-fibrillar matrix, respectively; $\mathbf{F}$ is the deformation gradient tensor; $J = \det(\mathbf{F})$ is its determinant; and $\mathbf{I}$ is the second-order identity tensor.

Given the non-fibrillar matrix modulus $E_{\mathrm{nf}}$ and non-fibrillar Poisson ratio $\nu_{\mathrm{nf}}$, the bulk and shear moduli are, respectively, expressed as:

$$K_{\mathrm{nf}} = \frac{E_{\mathrm{nf}}}{3(1 - 2\nu_{\mathrm{nf}})}, \quad G_{\mathrm{nf}} = \frac{E_{\mathrm{nf}}}{2(1 + \nu_{\mathrm{nf}})} \tag{5.3}$$

## 5.2. Fibrillar matrix

The Benninghoff arcade model (Figure 5.1) describes the organization of collagen fibrils as a function of depth in the AC [19, 28, 44]. This experimentally observed architecture is modeled as bundles of primary fibrils that split into different families bending radially and circumferentially [13]. The relative thicknesses of the superficial, middle, and deep zones in AC are defined based on histological analysis [14]. Since collagen content varies throughout the tissue [56], a depth-dependent fibril volume density $\rho_z$ is introduced [13].

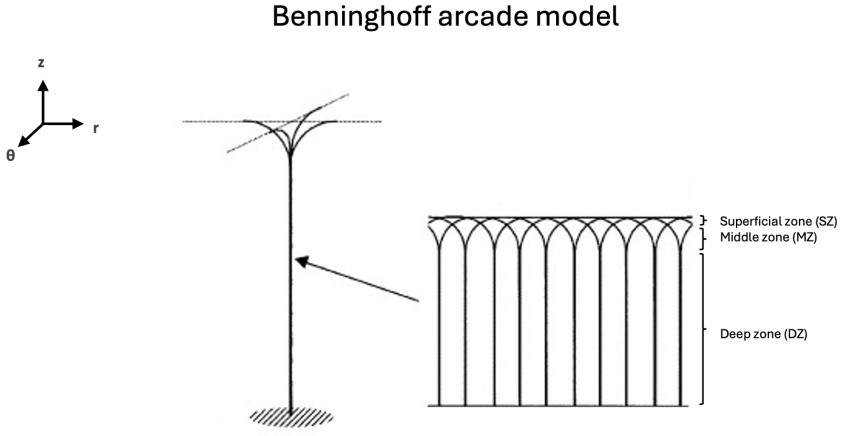


Figure 5.1: Schematic representation of a single primary collagen fibril bundle and its depth-dependent orientations according to Benninghoff arcade model. Adapted from [13].

Furthermore, in order to account for dispersion, a randomly oriented isotropic network of sec-

ondary collagen fibrils is included [13, 39] (Figure 5.2). The number and orientation of fibrils contribute to the local stiffness [13]; the greater the number of fibrils aligned along a specific direction, the higher the stiffness and resistance to deformation in that direction.

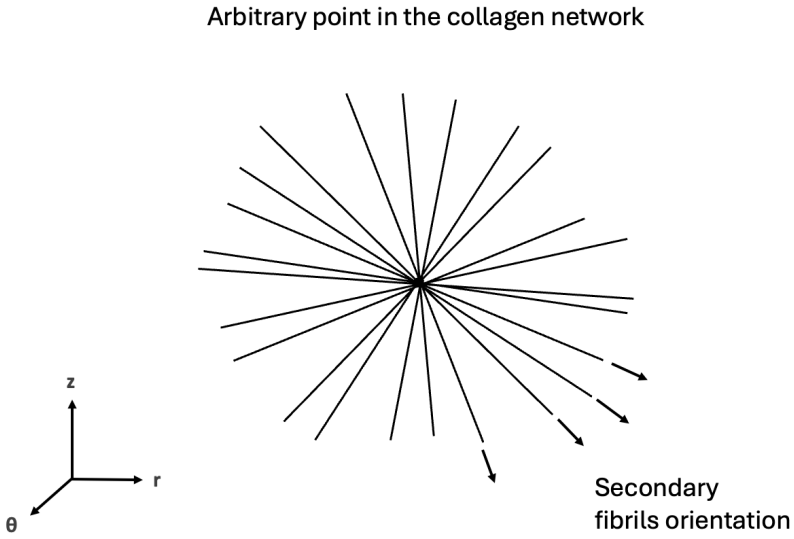


Figure 5.2: Schematic representation of the random orientation of secondary collagen fibrils. Adapted from [13].

The mechanical behavior of primary and secondary collagen fibrils is represented through a mechanical analogue illustrated in Figure 5.3, consisting of a linear elastic spring with stiffness $E_0$, arranged in parallel with a non-linear spring of strain-dependent stiffness $E_1 = E_\varepsilon \varepsilon_f$, where $E_\varepsilon$ is a positive material constant and $\varepsilon_f$ the fibril strain [9, 13, 16, 70].

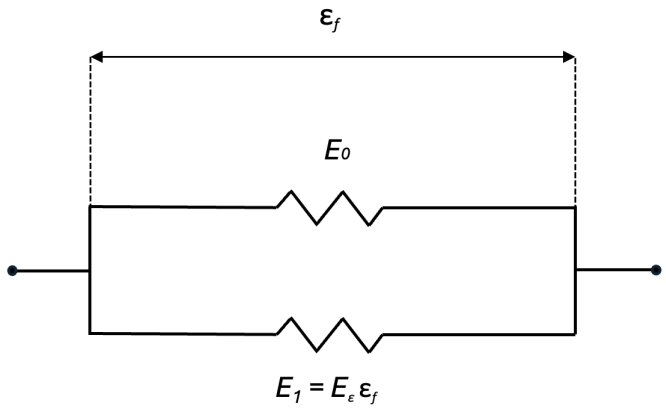


Figure 5.3: Schematic representation of the mechanical behavior of a collagen fibril.

Assuming that the fibrils can bear only tensile loads ($\varepsilon_f > 0$), the fibrillar stress $\sigma_f$ is expressed as follows [9]:

$$\sigma_f = \begin{cases} 0, & \text{if } \varepsilon_f \leq 0 \\ \frac{1}{2} E_f^{\varepsilon} \varepsilon_f^2 + E_f^0 \varepsilon_f, & \text{if } \varepsilon_f > 0 \end{cases} \tag{5.4}$$

In the present FRPE, the collagen network consists of 4 primary fibrils and 13 secondary fibrils, based on [13]. In line with previously reported values [14], the ratio between primary and secondary fibrils is set to $C = 12.16$. Furthermore, the collagen density is assumed to vary with the normalized depth $z^*$ of the tissue, using the following profile [72, 73]:

$$\rho_f(z^*) = 1.4(z^*)^2 - 1.1z^* + 0.59 \tag{5.5}$$

where $z^*$ is equal to 0 at the articular surface and equal to 1 at the interface with the calcified cartilage layer.

Therefore, the total stress tensor within the fibrillar matrix can be obtained by summing the contributions of all fibrils acting along different orientations [9, 39]:

$$\boldsymbol{\sigma}_f = \sum_{i=1}^{f_{\text{tot}}} \sigma_{f,i}\, \mathbf{e}_f \otimes \mathbf{e}_f, \tag{5.6}$$

where $f_{\text{tot}}$ is the total number of fibrils considered in the model, $\sigma_{f,i}$ is the scalar stress of each individual fibril, $\mathbf{e}_f$ is the fibril orientation unit vector, and $\otimes$ denotes the outer product.

Considering that the model includes both primary and secondary collagen fibrils, the scalar fibril stress $\sigma_{f,i}$ in Equation 5.6 is defined according to the corresponding fibril family as follows:

$$\sigma_{f,p} = \rho_z\, C\, \sigma_f, \qquad \sigma_{f,s} = \rho_z\, \sigma_f, \tag{5.7}$$

where $\sigma_{f,p}$ and $\sigma_{f,s}$ represent the stresses generated by the primary and secondary fibrils, respectively, and $C$ is the ratio between primary and secondary fibril density. These expressions are included in the summation of Equation 5.6 to obtain the total fibrillar stress tensor.

## 5.3. Interstitial fluid

When the AC is compressed, the pore volume within its solid matrix decreases. This reduction in porosity results in decreased permeability [53]. A parameter describing this behavior is the void ratio $e$, defined as the ratio between the volume of fluid $n_f$ and the volume of the solid matrix $n_s$:

$$e = \frac{n_f}{n_s} \tag{5.8}$$

Based on current and initial void ratios $e$ and $e_0$, the strain-dependent permeability can be formulated as follows [13, 39, 65]:

$$k = k_0 \left( \frac{1+e}{1+e_0} \right)^M , \tag{5.9}$$

where $k$ and $k_0$ represent the current and initial permeability, and $M$ is a positive dimensionless constant known as permeability strain dependency coefficient.

In the present model, Darcy's law (Equation 4.1) governs the fluid flow, with permeability assumed to vary according to Equation 5.9. Based on previous studies [56, 74], the water fraction $n_f$ is assumed to decrease with depth and is defined as:

$$n_f(z^*) = 0.80 - 0.15z^* \tag{5.10}$$

# 6 | Materials and methods

This thesis explored the feasibility of non-fibrillar Poisson's ratio determination in knee AC using a fiber-reinforced material model.

For each successfully tested sample, the main steps summarized in Figure 6.1 were performed. The first step consisted of the analysis of the experimental data obtained from previously performed mechanical tests. To this aim, the image data and the recorded force measurements were processed. Image segmentation was carried out to evaluate AC lateral expansion, while the force-time curve was extracted from the experimental measurements. The second step consisted of the identification of the material model parameters. To this aim, an idealized finite element model of the AC sample was developed, together with an iterative method to fit computational results to the experimental data for the sake of identifying the constitutive parameters by reverse engineering. The idealized model was used to simulate the experimental protocol, and the constitutive parameters were identified by fitting the numerical response to the corresponding experimental results. The third step consisted of a validation procedure. The agreement between experimental and computational results was evaluated against a predefined acceptance threshold. If the idealized model with the identified constitutive parameters did not allow to accurately reproduce the experimental response, the same test was simulated through the sample-specific model to i) check if experimental data were well reproduced when the non-idealized geometry of the sample was accounted for and ii) finally identifying the sample-specific constitutive parameters by a further fitting process.

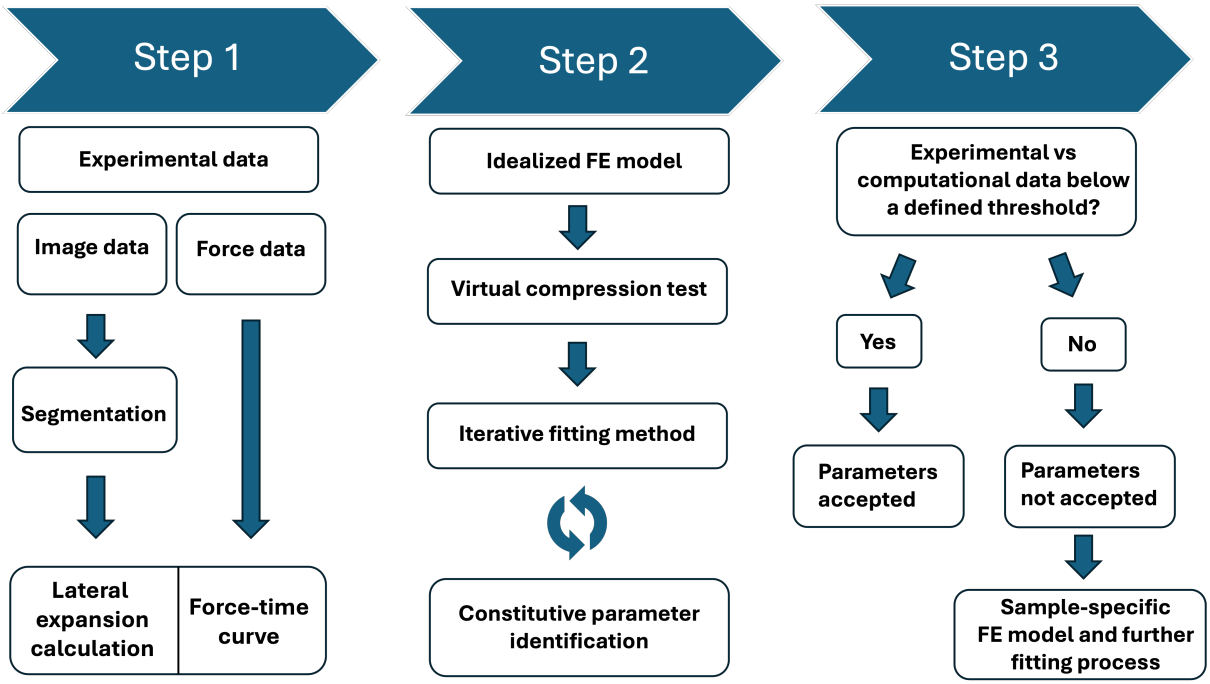


Figure 6.1: Overview of the main steps of the thesis workflow.

## 6.1. Experimental data

The experimental dataset used in this study was acquired as part of a proof-of-concept study performed at the TOMCAT beamline (Swiss Light Source, Paul Scherrer Institute, Switzerland [22]) by the Lund Biomechanics research group, prior to the beginning of this thesis work. Healthy AC tissue samples, in the form of cylinders 4 mm in diameter, were obtained from the femoropatellar groove of a bovine knee joint. Time-resolved synchrotron-based X-ray phase-contrast micro-computed tomography (SR-PhC-$\mu$CT) was used to investigate tissue behavior. This imaging technique exploits differences in refractive index to enhance soft tissue contrast, thereby eliminating the need for staining or contrast agents. Thanks to its high acquisition speeds, both static and time-resolved (4D) tomographic imaging can be performed, allowing for real-time analysis of tissue microstructural responses to mechanical loading [22]. This setup produced projection images with a resolution of 2.75 $\mu$m per pixel, resulting in a total imaging area of 5.54 $\times$ 3.85 mm$^2$ (2016 $\times$ 1400 pixels). More details are available in [22].

Unconfined compression with a stress-relaxation protocol was employed to test the samples. A 2 N preload was applied gradually over 15 s to guarantee uniform contact between the sample and the testing plates, followed by a 300 s relaxation period at constant displacement. Subsequently, two displacement steps were imposed, each corresponding to 15% strain at a loading rate of 1% s$^{-1}$. The displacement magnitude for each step was obtained based on the sample height measured from the tomographic projections acquired after preloading. After each compression step, the load was held for 600 s and 900 s, respectively, to allow stress-relaxation. During

the test, force–time curves were recorded. A total of fifteen dynamic scans (5 s per scan) were obtained during loading and relaxation phases, whereas two static scans (40 s per scan), providing the highest image quality, were recorded before the preload and after the second relaxation phase, respectively.

The testing protocol is illustrated in Figure 6.2.

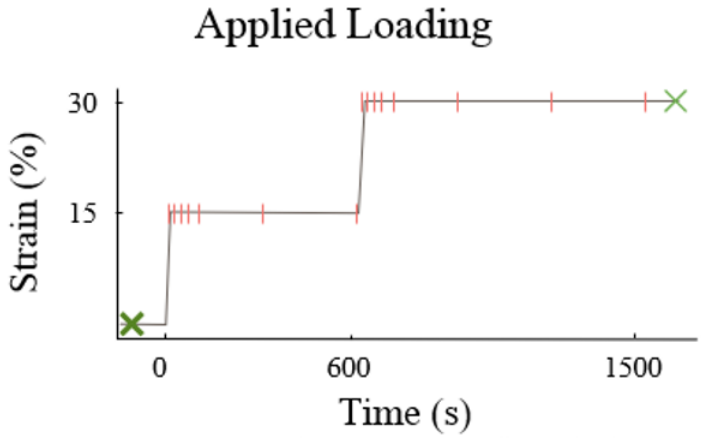


Figure 6.2: Schematic of the stress-relaxation protocol used for AC samples testing. Green crosses indicate static scans, while red bars represent dynamic scans. Adapted from [22].

## 6.2. Image data

A total of eight samples were tested using a stress-relaxation protocol [22]. Since parameter identification is the primary aim of the present analysis, the selection of the specimens included in the workflow was based on the following criteria: (i) presence or absence of calcified cartilage and subchondral bone, (ii) irregular geometry or macroscopic defects (e.g, missing cartilage), and (iii) correct adherence to the loading plate during mechanical testing. Previous work has shown that both residual calcified tissue and geometric imperfections consistently affect the mechanical response of AC in unconfined compression, altering peak and equilibrium forces and introducing variability unrelated to the intrinsic material properties [75]. Consequently, this can bias the fitted material parameters. The selection was carried out by analyzing the previously acquired tomographic datasets in ImageJ [76].

The results of this qualitative screening are summarized in Table 6.1.

| Sample ID | Observation | Included in analysis |
|---|---|---|
| 01 | Limited presence of bone | ✓ |
| 02 | Absence of bone; bent geometry | ✓ |
| 03 | Consistent presence of bone; slit in cartilage | – |
| 04 | Missing cartilage tissue; poor adherence to the loading plate | – |
| 05 | Presence of residual bone; missing cartilage; poor adherence to the loading plate | – |
| 06 | Subchondral bone was not detached, constraining expansion | – |
| 07 | Subchondral bone was not detached, constraining expansion | – |
| 08 | Subchondral bone was not detached, constraining expansion | – |

Table 6.1: Summary of the available specimens tested in stress-relaxation experiment [22], with related observations and assessment for their suitability for the analysis.

Tomographic images of the two selected samples in their unloaded configurations are presented in Figure 6.3. Additionally, dynamic images for sample 02 are provided in Figure 6.4, showing its response after 15% and 30% strain. Figure 6.5 illustrates the main irregularities observed in the available bovine AC samples.

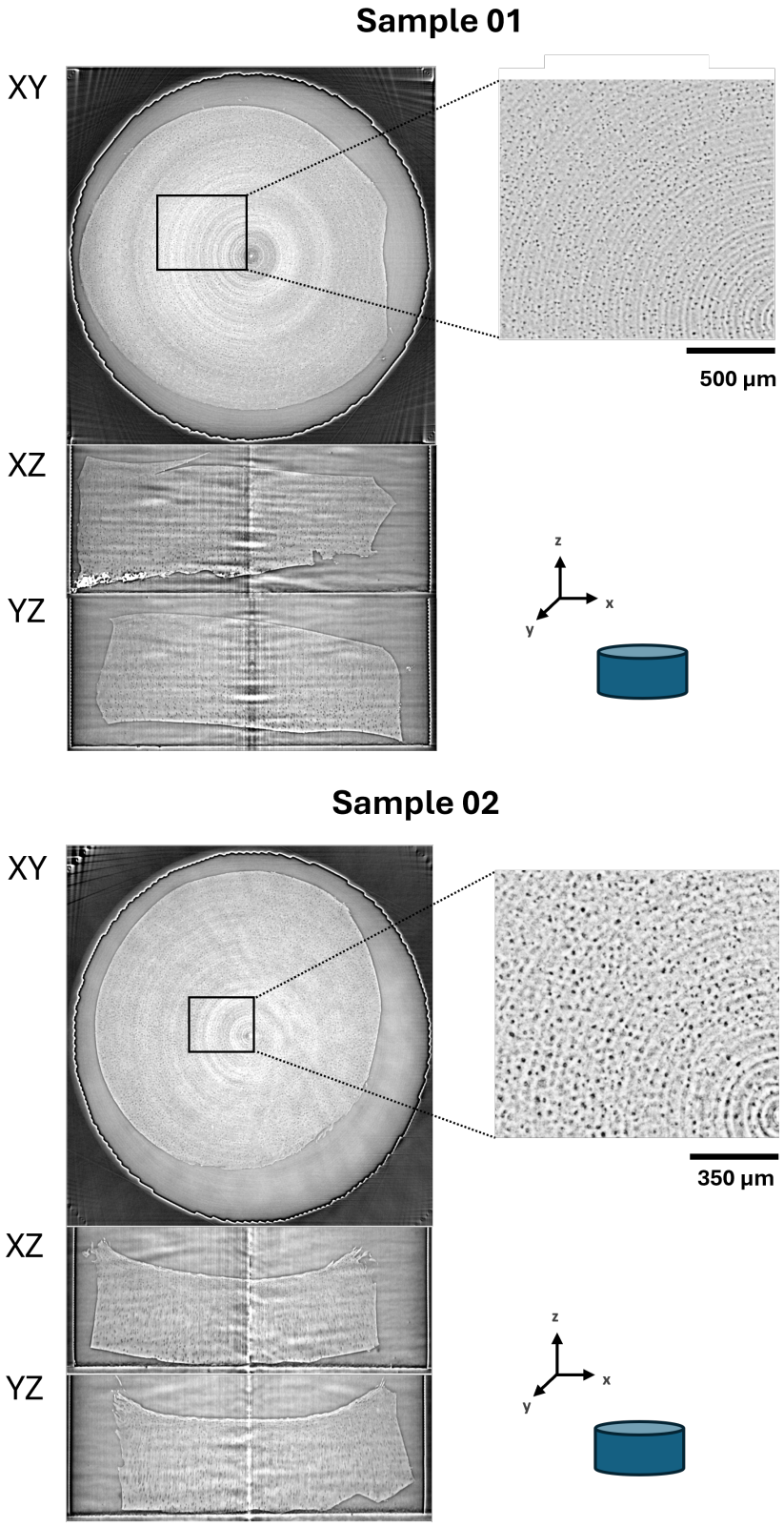


Figure 6.3: Orthogonal static views (XY, XZ, YZ planes) of sample 01 and 02. Two enlarged insets are provided to improve the visualization of chondrocytes.

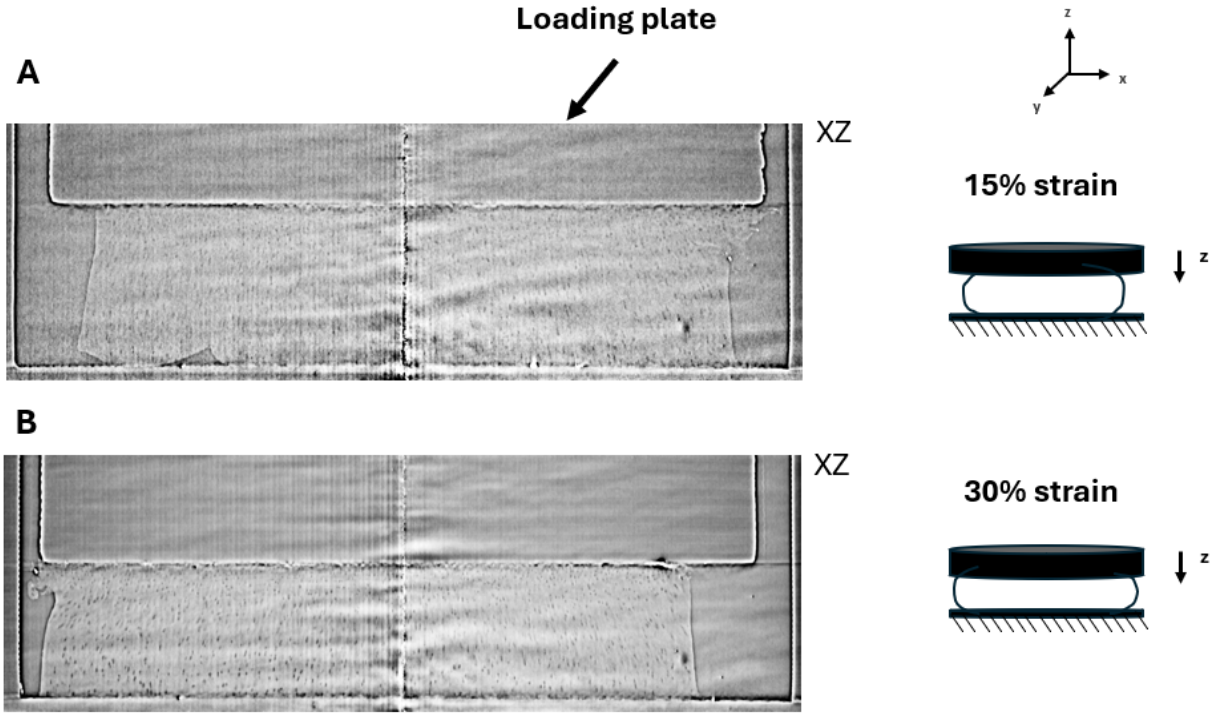


Figure 6.4: XZ orthogonal dynamic views showing the response of sample 02 after 15% and 30% compression.

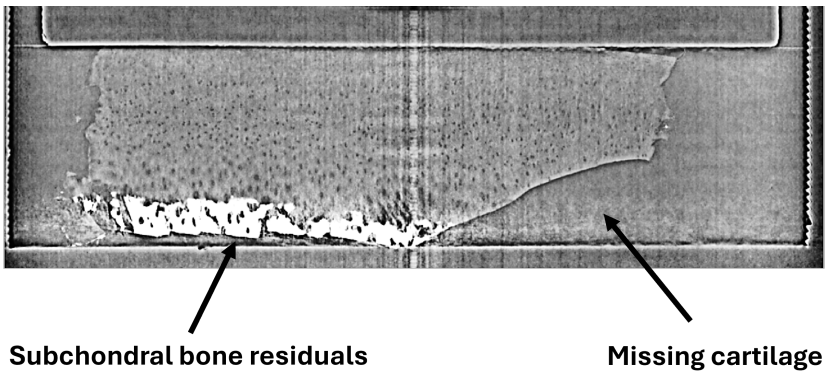


Figure 6.5: Schematic representation of the main irregularities observed in bovine AC samples. Data shown refers to the 7th dynamic scan of sample 04 (see Table 6.1). Similar irregularities have been observed in previous studies [75].

The lateral expansion under compression of the two selected samples was subsequently evaluated by measuring the cross-sectional area from top-view (XY-plane) images at three key time points: the first static scan, representing the initial undeformed condition; the last dynamic scan of the first relaxation period, representing the first equilibrium deformed condition; and the final static scan, representing the second equilibrium deformed condition. These scans were selected from Figure 6.2. While static scans served as reference states, dynamic scans provided the opportunity

to explore AC behavior at equilibrium.

For each sample, the analysis was performed by first identifying the middle of the specimen through the tomographic image stack in ImageJ. Around this central position, 100 consecutive slices were considered to capture a representative region of the tissue. This approach was chosen to reduce the risk of local variations in cross-sectional area, and thereby to obtain a more robust estimation of the lateral expansion between static and dynamic configurations.

The cross-sectional area was then obtained through manual segmentation of the tissue in ImageJ every 10 slices, as shown in Figure 6.6:

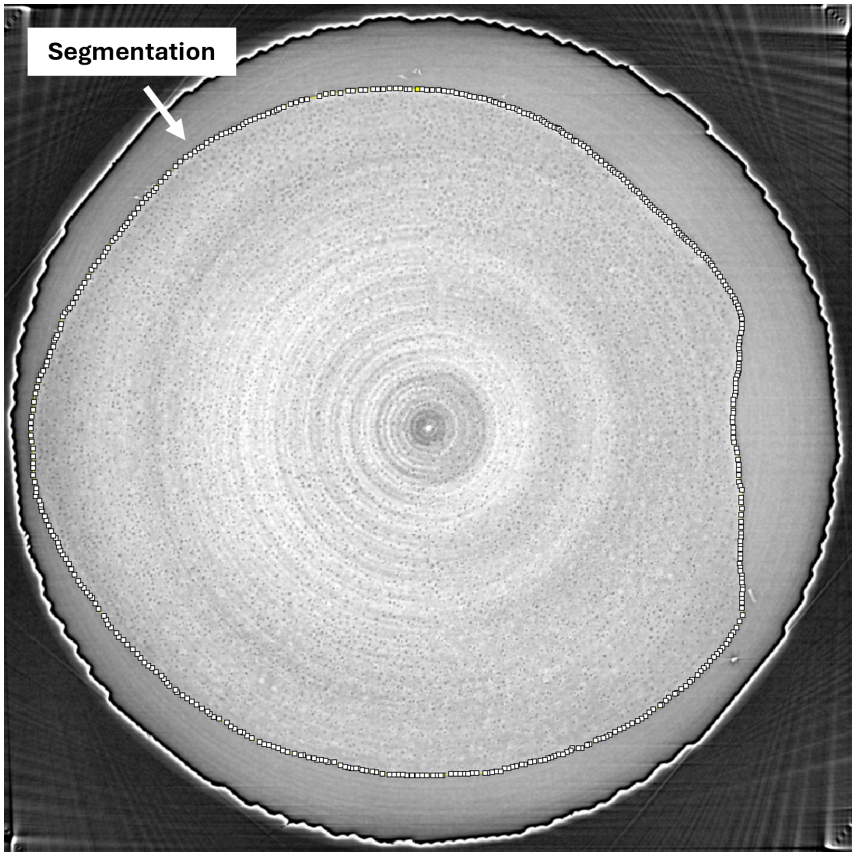


Figure 6.6: Example of manual segmentation in ImageJ for a slice of sample 02. The white dots represent the polygon vertices selected to delineate the tissue boundary during segmentation.

The average of these measurements was used as the representative cross-sectional area for that specific configuration. This procedure was repeated for all three configurations described above, obtaining the lateral expansion of the sample at different steps of the testing protocol.

As the samples were immersed in phospate-buffered saline (PBS), they were partially floating within the chamber. As a result, one of the two specimens (sample 01) was not properly aligned with the loading plates in the static configuration. To ensure consistent cross-sectional analysis, a preliminary 3D reorientation of the static image stack was required. The alignment correction

was performed in DataViewer, using the dynamic scan acquired under load as spatial reference and the static scan as target of reorientation.

## 6.3. Idealized FE model

Two idealized FE models representing AC tissue were developed as cylindrical geometries with a diameter of 4 mm and heights of 1.39 mm and 1.01 mm, respectively. The FRPE material model discussed in Chapter 5 was assigned to the idealized geometries as a user-defined material (UMAT) in ABAQUS/Standard (Version 2023, SIMULIA, Dassault Systèmes) [13, 56, 74]. The cylinders were discretized using 8-nodes poroelastic hexahedral elements (C3D8P) with characteristic dimensions of 0.18 mm and 0.25 mm, respectively, which were set upon mesh convergence analysis. Appropriate boundary conditions were assigned to reproduce the unconfined compression and stress-relaxation testing protocols described above (Figure 6.7). To prevent rigid body motion without restricting radial expansion, four lateral nodes were constrained: two along the Y-axis in X direction, and two along the X-axis in Y direction. Free fluid flow (e.g, null pore pressure) was allowed through the lateral surfaces, while the top and bottom surfaces of the model were assumed to be impermeable. A time-dependent downward vertical displacement was imposed on the nodes of the top surface to reproduce the strain history represented in Figure 6.2.

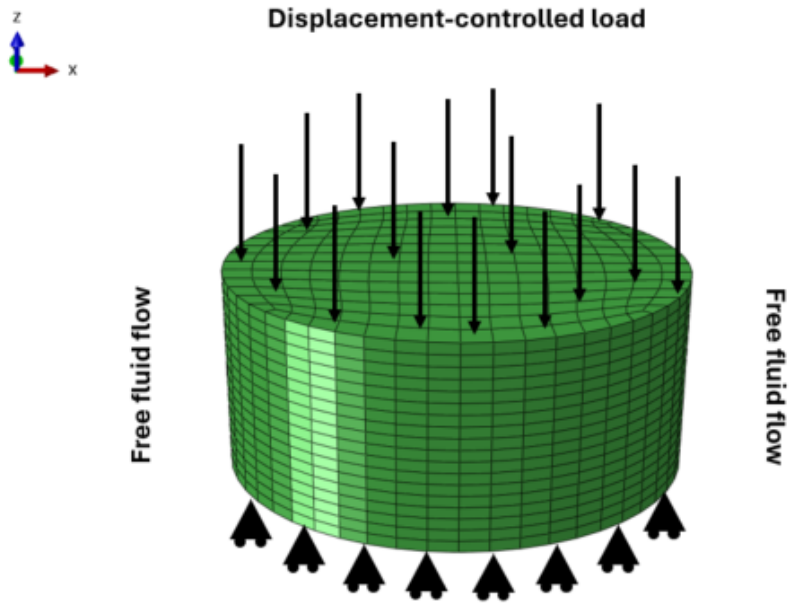


Figure 6.7: Idealized FE model of AC showing boundary conditions for displacement-controlled load on the top surface, constrains at the bottom surface, and free fluid flow through the lateral surfaces.

## 6.4. Material properties

The FRPE material model adopted in this study is described by seven parameters: the Young's modulus of the non-fibrillar matrix $E_{\mathrm{nf}}$, its Poisson ratio $\nu_{\mathrm{nf}}$, the Young's moduli of the linear and non-linear fibrillar components $E_0$ and $E_{\mathrm{fe}}$, respectively, the initial permeability $K_0$, the strain-dependent permeability exponent $M$, and the ratio between primary and secondary collagen fibrils $C$ (Table 6.2). All material parameters, except for $C$, were identified by fitting the model to the experimental data to allow the estimation of $\nu_{\mathrm{nf}}$, while also optimizing the remaining parameters to obtain the optimal match between the experimental and numerical data (Table 6.2).

| Parameter | Description | Unit | Range |
|---|---|---|---|
| $E_{nf}$ | Young's modulus of the non-fibrillar matrix | MPa | 0.1 - 1 |
| $\nu_{nf}$ | Poisson's ratio of the non-fibrillar matrix | – | 0.15 - 0.48 |
| $E_0$ | Young's modulus of the linear fibrillar spring | MPa | 0.3 - 10 |
| $E_{fe}$ | Young's modulus of the non-linear fibrillar spring | MPa | 40 - 400 |
| $k_0$ | Initial permeability | $\mathrm{mm}^4/\mathrm{N{\cdot}s}$ | 0.0001 - 0.01 |
| $M$ | Exponent for strain-dependent permeability | – | 1 - 12 |
| $C$ | Primary to secondary fibrils ratio | – | 12.16 |

Table 6.2: Material model parameters and optimization ranges [9, 13, 14, 75]. In line with previous studies [13, 14], the parameter $C$ value was fixed.

The fitting pipeline developed in this work simultaneously minimized the error in both the reaction force and lateral expansion (quantified through areal strain), enabling to capture both the axial and transverse responses of AC.

The optimization routine was implemented as an iterative process that combines MATLAB and ABAQUS. Starting from an initial guess within the predefined parameter ranges, each iteration consisted of the following steps (Figure 6.9):

(i) automatic assignment of the current parameter set to the UMAT and run of the unconfined compression stress-relaxation simulation;
(ii) automated data extraction through Python scripts, obtaining the reaction forces at the top surface and the lateral expansion at time points corresponding to the experimental measurements. The lateral expansion was quantified as the areal strain computed on a central box of the model (corresponding to 10% of the sample height) using the *ConvexHull* function in Python. This function calculates the area of the smallest convex polygon enclosing all the nodes projected onto the XY plane (Figure 6.8).

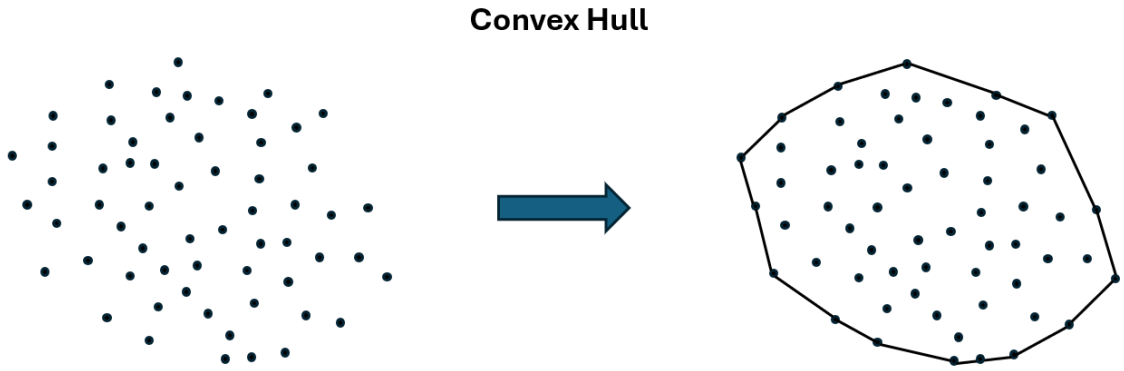


Figure 6.8: Schematic representation of *ConvexHull* algorithm. Given a set of points, the convex hull is defined as the smallest convex polygon that contains all the points.

(iii) computation of the error, quantified through the normalized root-mean-square error (RMSE) between experimental and numerical curves. The normalized RMSE was calculated as:

$$\text{Normalized RMSE} = \sqrt{\frac{1}{N}\sum_{i=1}^{N}\left(\frac{\hat{y}_i - y_i}{y_i}\right)^2}$$

where $\hat{y}_i$ is the predicted value (model), $y_i$ the corresponding target value (experiment), $N$ the number of points considered on the curve.

A weighted total RMSE was then defined as:

$$RMSE_{\text{tot}} = w_f \cdot RMSE_{force} + w_s \cdot RMSE_{strain} \tag{6.1}$$

where the weighting coefficients $w_{\text{f}}$ and $w_{\text{s}}$ represent the relative contribution of the force and areal strain components to the objective function;

(iv) error evaluation and parameters update, where $RMSE_{\text{tot}}$ was compared with a predefined tolerance. If the criterion was not satisfied, the parameters were iteratively updated until convergence. Upon an initial analysis of different methods, the minimization of $RMSE_{\text{tot}}$ was implemented through the Globalized-Bounded Nelder-Mead ($GBNM$) algorithm [77]. This approach automatically restarts the optimization with a new unique initial guess once a local minimum is reached, thereby enhancing the likelihood of finding the global minimum and improving the overall robustness of the analysis (Figure 6.9).

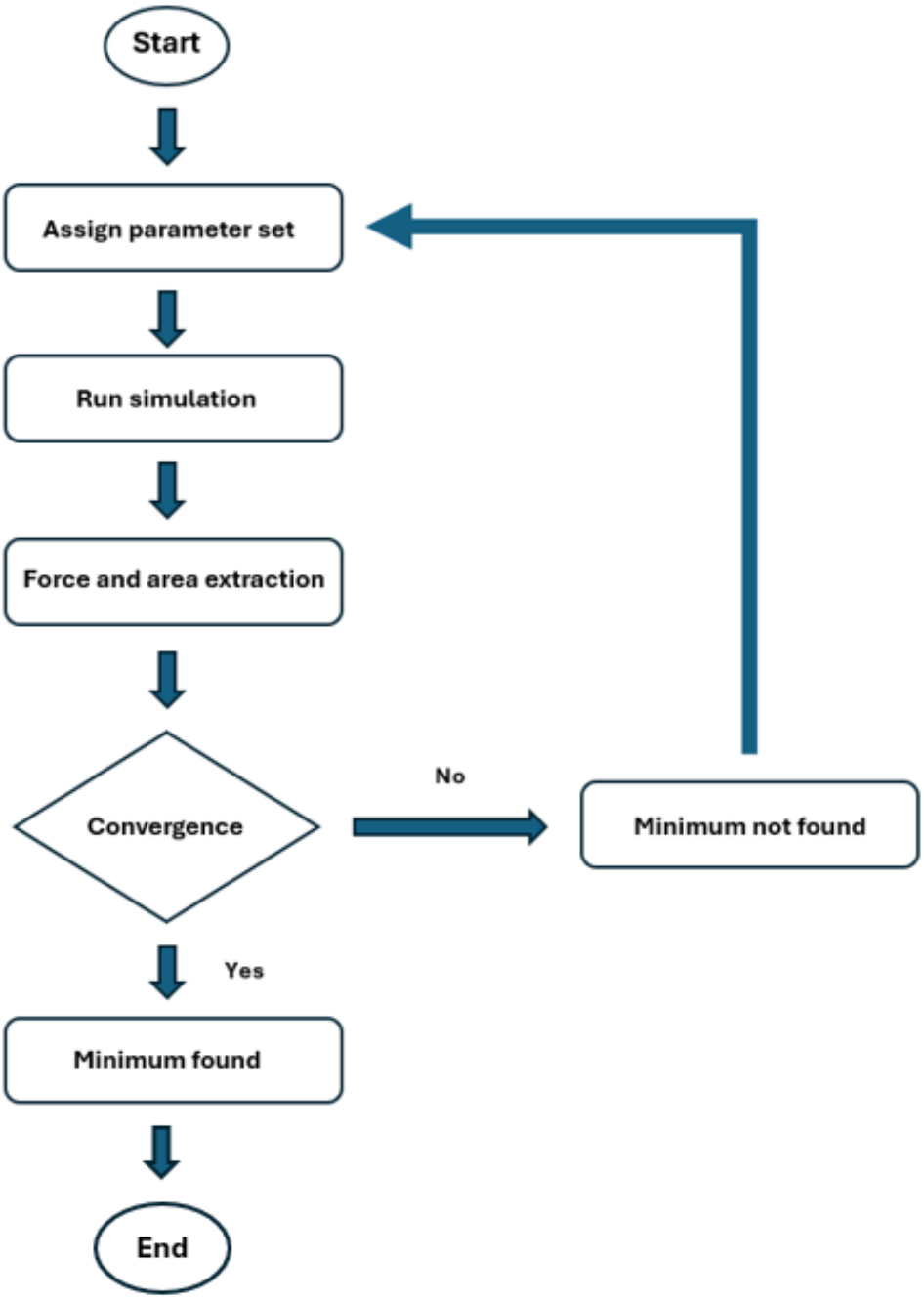


Figure 6.9: Fitting workflow corresponding to a single restart of the GBNM-based routine. A new initial guess is automatically generated after convergence, resulting in a continuous loop.

After a series of preliminary tests, it was observed that assigning equal weights to reaction force and cross section ($w_{\mathrm{f}} = w_{\mathrm{s}} = 0.5$) provided the most balanced calibration. $RMSE_{\mathrm{tot}}$ was computed over selected time points across the entire stress-relaxation profile, including both peak and equilibrium phases, as shown in Figure 6.10.

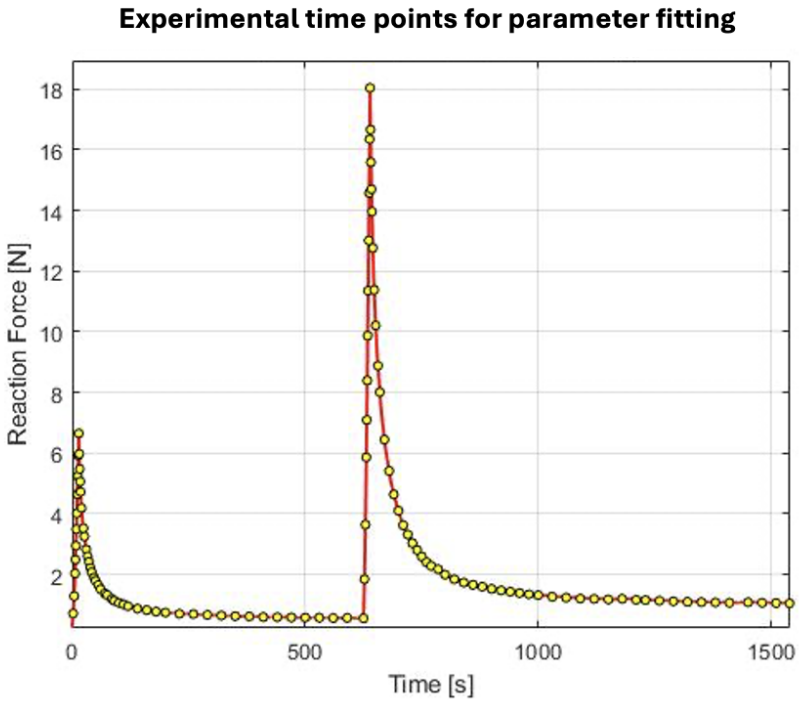


Figure 6.10: Experimental reaction force-time curve (red line). The yellow markers indicate the selected experimental data time points used for the fitting procedure and computation of the objective function.

## 6.5. Sample-specific model

A sample-specific FE model was developed to reproduce the experimental conditions and evaluate the material parameter fitting on a realistic geometry. This model was implemented only for specimen 02, as the corresponding idealized configuration showed deviations from the experimental behavior. To generate the discretized geometry of the sample, the tomographic images of the real sample were semi-automatically segmented using 3D Slicer and Seg3D [78, 79]. The geometry reconstructed from the segmentation mask was discretized into linear tetrahedral elements with 0.15 mm characteristic dimension in ANSA v24.1.2, BETA CAE (Figure 6.11A). The resulting elements were defined as C3D4P elements for coupled pore-pressure analyses in ABAQUS. The element size was selected to balance geometric accuracy and computational cost. Both mesh quality and convergence were assessed.

To prevent rigid body motion while allowing for lateral expansion, the same strategy applied in the idealized model (Figure 6.7) was applied to the sample-specific model (Section 6.3). Under loading, the constrained regions did not exhibit abnormal stress levels, confirming that the prescribed constraints did not introduce artifacts or influence the behavior of the model. On the other hand, vertical compression was simulated through a different approach compared to the one adopted for the idealized cylindrical sample: the sample was positioned between two

rigid plates, modeled as discrete rigid bodies. A frictionless node-to-surface contact formulation was defined between the sample and the plates [75]. The upper plate was prescribed a vertical downward displacement whose magnitude was estimated from the $\mu$CT scans, while the lower plate was fully constrained in all degrees of freedom. Both contact surfaces were assumed to be impermeable to fluid flow. This strategy allowed to cope with the non-planar geometry of the sample surfaces.

The elements were assigned the same user-defined material adopted for the idealized sample model. In order to fit the material parameters on the experimental data, the same optimization pipeline described in Section 6.4 was applied.

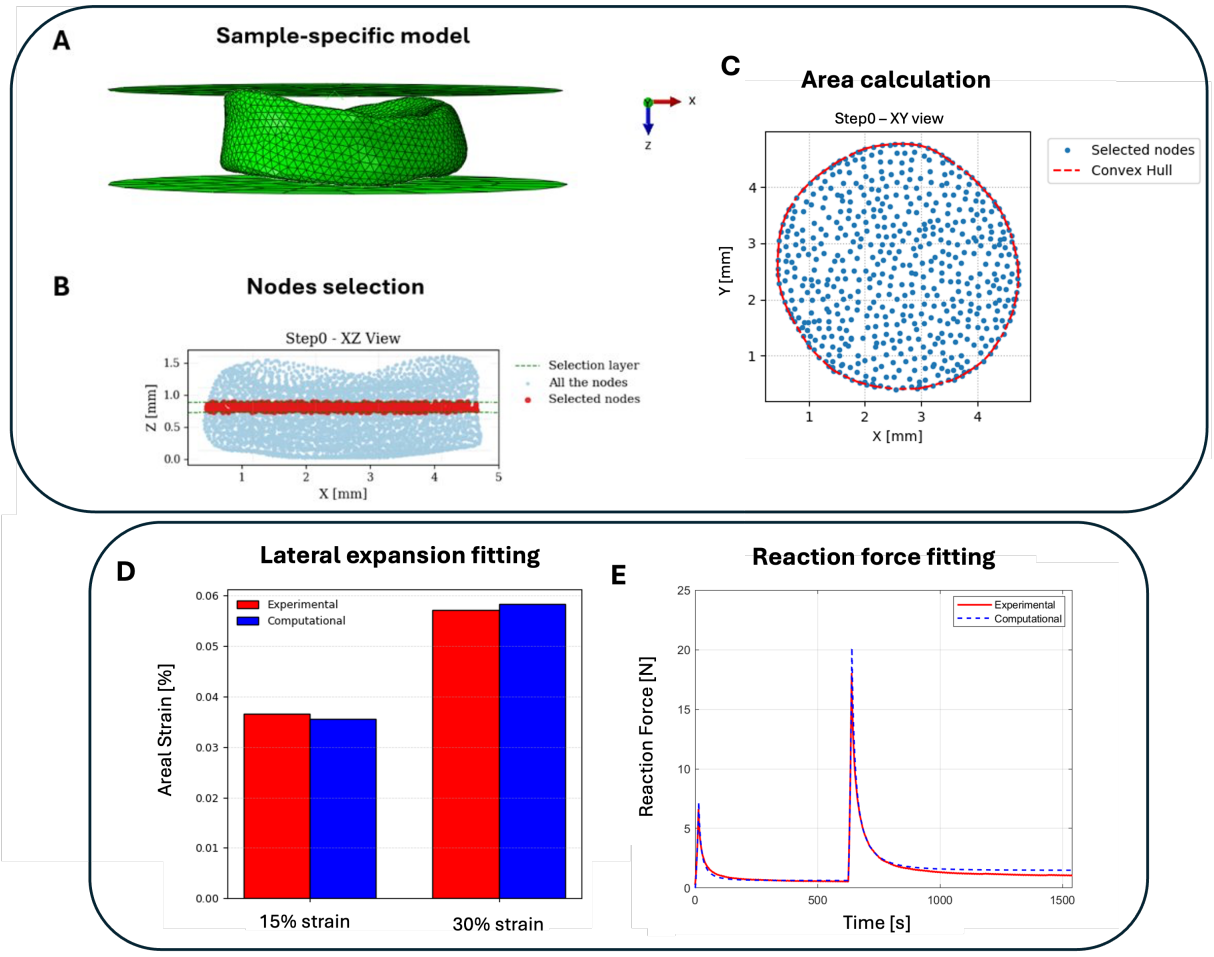


Figure 6.11: Overview of the sample-specific model and fitting procedure. A) The sample-specific model (ID 02). B) XZ view showing the nodes selection process. C) XY view describing the area calculation method. D) Example of lateral expansion fitting, where cumulative strains are illustrated. E) Example of reaction force fitting.

# 7 | Results

## 7.1. Experimental areal strain evaluation

The total lateral expansion values reported in Table 7.1 reflect the response accumulated over the full stress-relaxation protocol. Across the two samples, the total areal strain reached approximately 5.7% for sample 01 and 7.4% for sample 02 (Table 7.1), corresponding to an average expansion by 6.6%. The largest contribution to the inter-sample difference in total areal strains was observed in the second compression step.

| **Step** | **Sample 01** | **Sample 02** |
|---|---|---|
| $1^{st}$ step | +3.66% | +3.37% |
| $2^{nd}$ step | +2.05% | +3.89% |
| **Total expansion** | **+5.71%** | **+7.38%** |

Table 7.1: Lateral expansion values (%) obtained measuring the $\mu$CT images for the two selected samples (more details in Section 6.2).

## 7.2. Constitutive paramer identification through the idealized finite element model

For sample 01, the idealized sample model with the identified constitutive parameters accurately reproduced the experimental response ($RMSE_{tot} = 0.084$) (Table 7.2; Figure 7.1A–B). The simulation with a sample-specific geometry was hence deemed unnecessary.

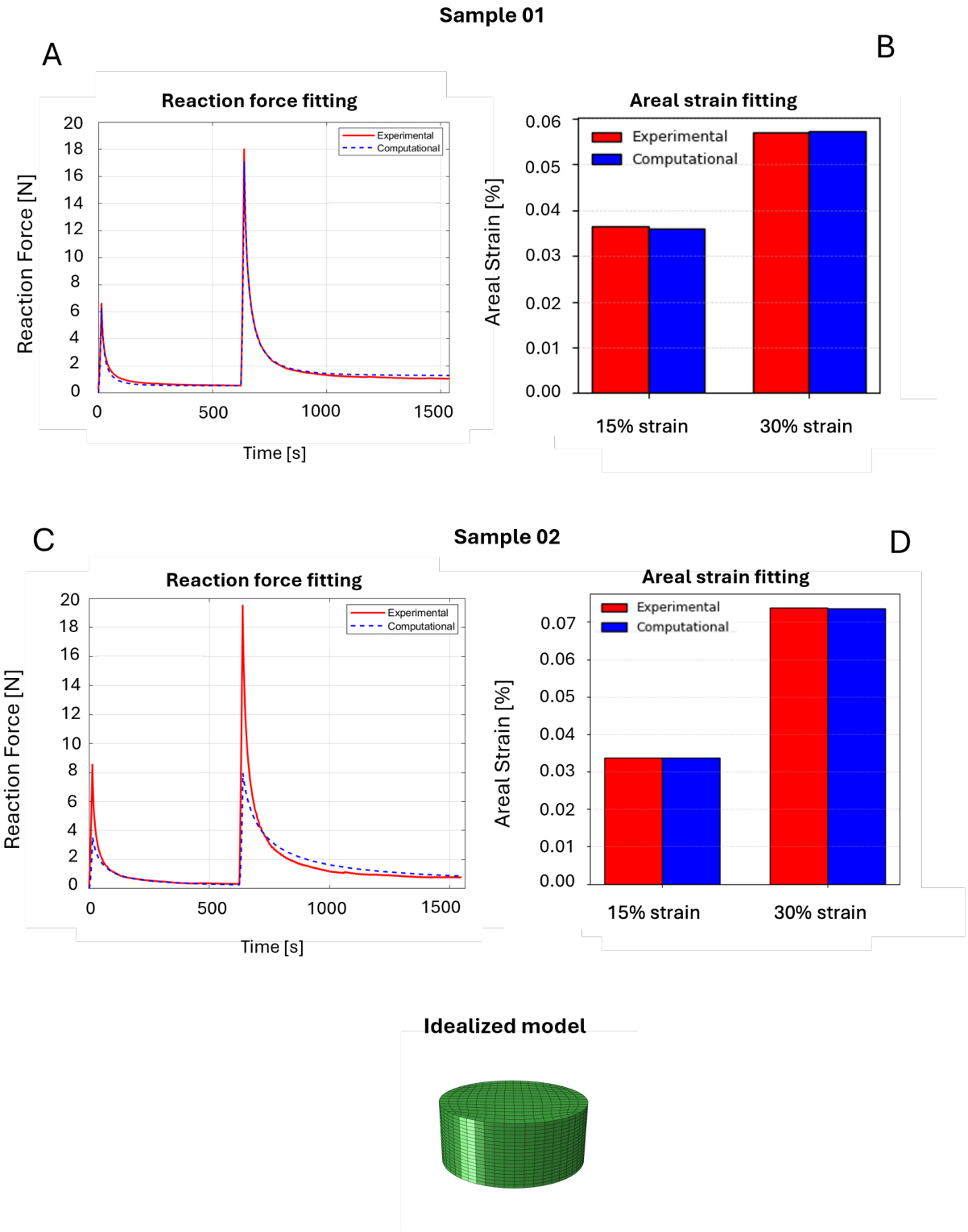


Figure 7.1: Results of the optimization for the idealized models of samples 01 and 02. A-B) Sample 01: simulated reaction forces fitted to the experimental stress-relaxation response (A) and lateral expansion fitting based on the areal strain computed between the undeformed configuration (1st static scan) and the deformed states after the first and second loading ramps (7th dynamic and 2nd static scans) (B). C-D) Sample 02: fitting results for reaction force (C) and lateral expansion (D), evaluated using the same deformation states as in sample 01. Quantitative deviations are summarized in Table 7.3.

In contrast, for sample 02 the idealized FE model with the identified constitutive parameters resulted in a higher combined RMSE ($RMSE_{tot} = 0.14$). While equilibrium forces were predicted with high accuracy (Figure 7.1C); Table 7.3), the model substantially underestimated the peak forces, exhibiting relative errors by around 60% (Figure 7.1C; Table 7.3). Lateral expansion was predicted with similarly high accuracy as in sample 01, with negligible deviations from the experimental areal strain values (Figure 7.1D; Table 7.3). Thus, further simulations were performed with the sample-specific geometry.

## 7.3. Fitting of the sample-specific model: sample 02

While the FRPE material model produced heterogeneous strain distributions due to its anisotropy, the idealized model exhibited a more homogeneous strain field than the sample-specific case (Figure 7.2). However, when the fitting was repeated using a sample-specific geometry for sample 02, the overall accuracy did not improve. The sample-specific case showed a $RMSE_{tot} = 0.16$, as shown in Figure 7.3A-B. The reaction force profile was slightly better than that obtained with the idealized model (Figure 7.3A). In particular, equilibrium forces were predicted with high accuracy (<1%) (Table 7.3), the underestimation of peak forces was less marked yet still significant (-39.0% and -51.1% for the first and second peak force, respectively) (Figure 7.3A; Table 7.3). The prediction of lateral expansion worsened compared to the idealized model, reaching an overall discrepancy of approximately 15% after the second compression (Figure 7.3B; Table 7.3).

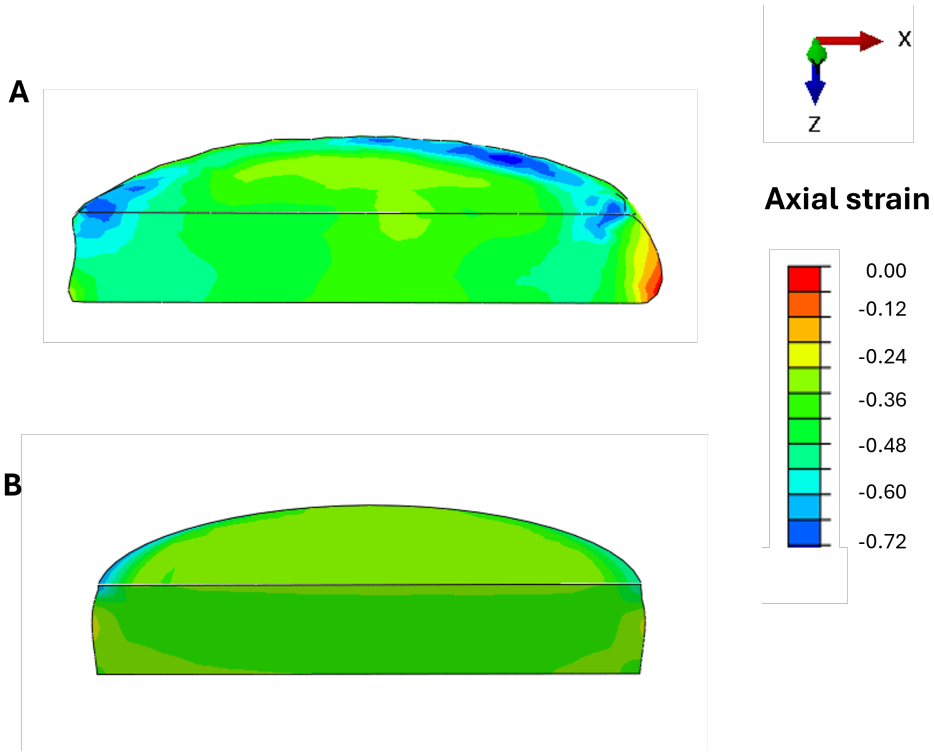


Figure 7.2: The axial logarithmic strain distribution is illustrated for both the sample-specific (A) and idealized (B) model of sample 02.

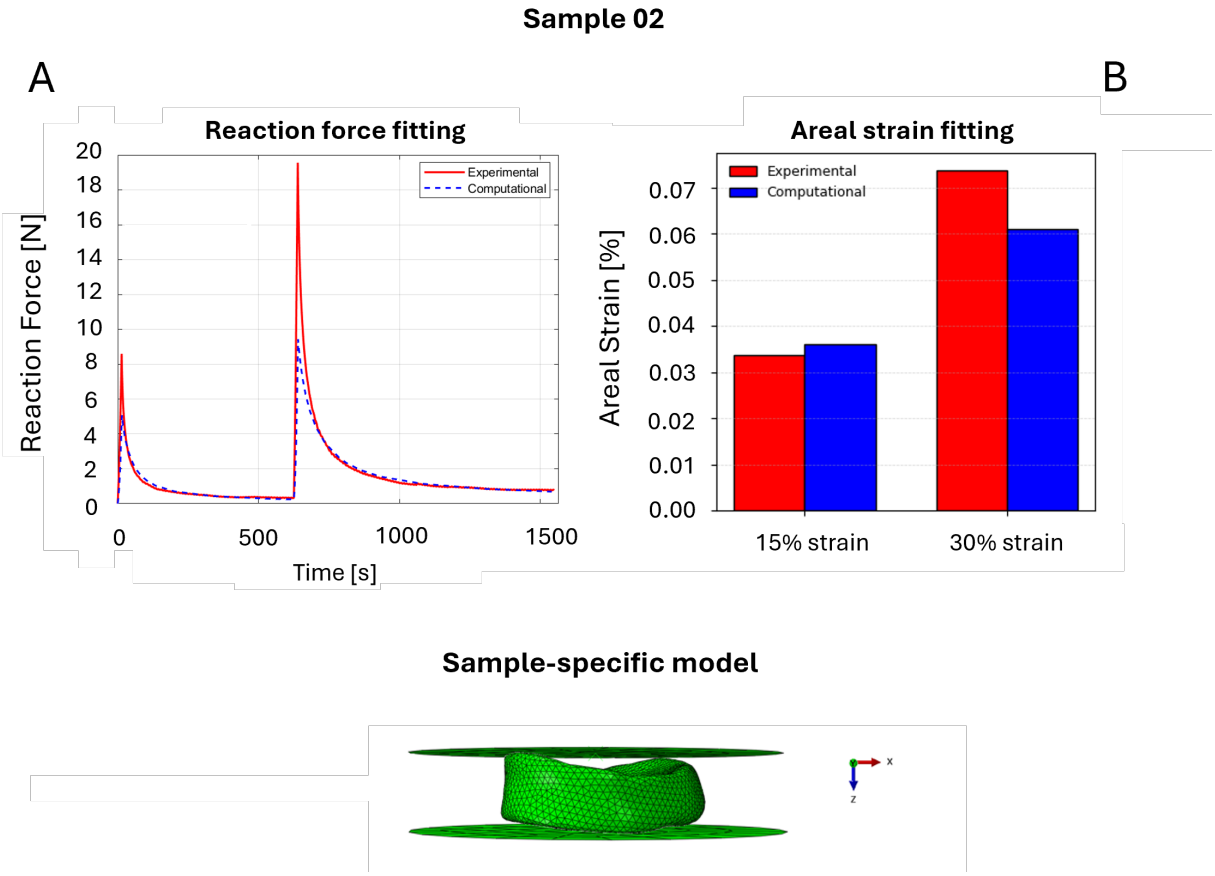


Figure 7.3: Results of the optimization for the sample-specific model of sample 02. A) Simulated reaction forces fitted to the experimental stress-relaxation response. B) Lateral expansion fitting based on the areal strain computed between the undeformed configuration (1st static scan) and the deformed states after the first and second loading ramps (7th dynamic and 2nd static scans). Quantitative deviations are summarized in Table 7.3.

The complete set of optimized parameters and relative differences for both samples are reported in Table 7.2 and Table 7.3 respectively.

| | $E_0$ (MPa) | $E_{nf}$ (MPa) | $\nu_{nf}$ (–) | $E_{fe}$ (MPa) | $k_0$ (mm$^4$/Ns) | $M$ (–) |
|---|---|---|---|---|---|---|
| **Idealized model (01)** | 0.12 | 0.063 | 0.46 | 271 | 0.010 | 6.83 |
| **Idealized model (02)** | 0.25 | 0.054 | 0.26 | 73 | 0.0057 | 8.16 |
| **Sample-specific model (02)** | 0.10 | 0.075 | 0.35 | 116 | 0.0091 | 5.85 |
| **Ebrahimi et al. [15]** | 0.86 ±0.46 | 0.29 ±0.15 | 0.42* | 4.01 ±3.69 | 0.0037 ±0.0028 | 9.84 ±3.85 |
| **Julkunen et al. [14]** | 0.92 ±0.33 | 0.22 ±0.1 | 0.22* | 150 ±113 | 0.006 ±0.0012 | 5.1 ±0.9 |

Table 7.2: Fitted FRPE material parameters for both idealized and sample-specific models. Literature data from [14, 15] are included for comparison. Values marked with * were fixed during the optimization. Note that Julkunen et al. employed a fibril-reinforced poroviscoelastic (FRPVE) material model.

| | **Peak force 1** | **Equilibrium force 1** | **Peak force 2** | **Equilibrium force 2** | **15% strain** | **30% strain** |
|---|---|---|---|---|---|---|
| **Idealized model (01)** | -6.8% | -4.2% | -5.5% | +18.4% | -2.8% | +2.0% |
| **Idealized model (02)** | -60.1% | -5.9% | -60.0% | -2.1% | <1% | <1% |
| **Sample-specific model (02)** | -39.0% | -12.5% | -51.1% | -7.1% | -8.2% | +15.5% |

Table 7.3: Relative differences (%) between the experimental and computational data for both reaction forces and areal strains at selected time points.

# 8 Discussion

The accurate identification of AC mechanical properties, such as Poisson ratio, is essential to perform accurate patient-specific FE simulations, which in turn could be used to improve the understanding of OA progression and to design targeted treatments. In this thesis work, a method for material parameter identification through FE simulation was developed and tested using experimental synchrotron-based data from stress-relaxation tests on AC samples. Unlike previous studies [9, 55], which used side views to estimate lateral displacement under loading, this work leveraged high-resolution tomographic images to track the lateral expansion throughout the loading protocol at key time points. As a result, the fitting procedure included both the reaction forces and the areal strain, offering the possibility of estimating non-fibrillar Poisson ratio.

## 8.1. Interpretation of the mechanical response

In the idealized models used for fitting, the areal strain was well captured in both samples, indicating an accurate representation of lateral expansion (Table 7.3). However, while sample 01 showed a good fit between experimental and simulated reaction force (Table 7.3), sample 02 underpredicted the peak forces in both the stress-relaxation cycles with the idealized model (Figure 7.1C; Table 7.3). In healthy AC, axial compression induces lateral expansion that is limited by the collagen network [55], resulting in increased fluid pressure that primarily governs the instantaneous response of the tissue [19, 28]. The model's underestimation of the peak force in sample 02 suggests that the constraining function of collagen network, and consequently, fluid pressurization, were not adequately captured.

Although both samples were taken from the same bovine knee, their mechanical response was different, resulting in up to 34% relative difference for the second equilibrium force and 30% for the overall areal strain. The inter-sample mechanical variability in AC was assessed already in a previous study [75]. As a consequence, each optimization problem involved different experimental data, resulting in different minima of the objective function and fitted material parameters for the two samples.

In sample 02, in order to fit the higher experimental areal strain compared to sample 01, the overall collagen stiffness decreased (Table 7.2), leading to lower pressurization and consequently reduced simulated peak forces. Furthermore, the fitting resulted in a lower initial permeability

$k_0$ and a higher strain-dependent permeability exponent $M$ (Table 7.2). As these two parameters have coupled effects—an increase in one can partially compensate for a decrease in the other—different combinations of ($k_0$, $M$) can produce similar macroscopic behaviors, making the identification of a unique pair challenging [80]. In the present case, $k_0$ and $M$ varied in opposite directions between idealized model 01 and model 02, preventing a clear interpretation of permeability-related effects on the peak response. In contrast, equilibrium forces were accurately captured in both idealized models (Table 7.3). At equilibrium, fluid flow has ceased and permeability no longer influences the response. The equilibrium behavior is governed by the non-fibrillar matrix, whose fitted stiffness differed by only 15% between the two samples (Table 7.2). The substantial decrease in non-fibrillar Poisson ratio $\nu_{\text{nf}}$ (0.46 to 0.26) from sample 01 is most likely the result of parameter compensation within the model, *i.e.*, the adjustment of one parameter to offset the effect of others during fitting. Since the fitted collagen stiffness and permeability parameters could not simultaneously reproduce both peak force and areal strain, the optimization shifted $\nu_{\text{nf}}$ toward low values to match the lateral expansion data. Such behavior, along with peak forse underestimation, suggests parameter compensation rather than true material properties, indicating that the parameter set obtained for sample 02 is not reliable. Conversely, the parameters fitted for sample 01—where both the stress-relaxation curve and areal strain were accurately reproduced—can be interpreted with greater confidence.

To examine whether accounting for the actual sample geometry could improve the fitting accuracy, a sample-specific model was developed for sample 02 (Figure 6.3). This specimen was selected because its idealized configuration, as previously discussed, exhibited larger deviations from the experimental response compared to sample 01, making it a suitable case to assess the influence of geometric idealization. When considering the sample-specific geometry, the overall quality of the fit worsened compared to the idealized cylindrical model, as indicated by an increase in $RMSE_{tot}$ (0.16 vs. 0.14). The reaction force profile showed an improvement, whereas the total areal strain was underestimated (Table 7.3). The additional spatial heterogeneities in the sample-specific geometry altered the local mechanical response and significantly affected the fitting process, resulting in optimized parameter variations ranging from -60% to +60% (Table 7.2). Despite these major variations in constitutive parameter values, the overall mechanical response of the sample-specific model remained comparable to the corresponding idealized case (Table 7.3). Compensatory adjustments among parameters, most notably between $E_0$ and $E_{fe}$, as well as $K_0$ and $M$, produced minor improvements in fluid pressurization during the transient phases but remained insufficient to reproduce the experimental peak forces (Table 7.2). Furthermore, the transition from idealized to sample-specific geometry led to a 60% increase in $E_{nf}$ and a 35% increase in $\nu_{\text{nf}}$ (Table 7.2). The stiffer non-fibrillar matrix likely contributed to the accurate prediction of the equilibrium forces (Table 7.3). Although an increase in $\nu_{\text{nf}}$ is generally associated with greater lateral expansion, the collagen fibrils constrained this effect, leading to an underestimation of the areal strain (Table 7.3). Notably, the fitted parameters for sample-specific model 02 showed greater similarity to those of idealized model 01, which

successfully captured both force and areal strain with high accuracy ($RMSE = 0.084$).

Direct comparison of the fitted material parameters with values reported in the literature is challenging due to differences in experimental protocols, material modeling, sample origin, and fitting objectives. Ebrahimi et al. [15] reported FRPE parameters fitted to human AC under indentation (Table 7.2). Two major factors limit direct comparability: (i) indentation primarily engages the superficial collagen fibrils oriented tangentially to the surface, whereas unconfined compression—as used here—primarily loads deeper, randomly oriented and perpendicular fibrils, which strongly influence lateral expansion [55], resulting in overall different collagen network recruitment and load-bearing behavior; and (ii) the biological source differs (human vs. bovine), with bovine AC generally exhibiting higher stiffness [81].

Given these considerations, comparisons were restricted to the idealized model of sample 01, which successfully reproduced both axial and lateral mechanical responses. Despite its geometric simplification, this model provides a suitable baseline for parameter analysis and is consistent with the idealized geometry adopted by Ebrahimi et al. [15]. Compared to their results, the fitted initial permeability $k_0$ was 170% higher, while the strain-dependent exponent $M$ was approximately 30% lower (Table 7.2), suggesting differences in fluid transport behavior. The higher permeability obtained in the present thesis may reflect the influence of the experimental setup. During indentation, the fluid is free to escape, but the compressed region is mechanically confined by the surrounding tissue, limiting lateral expansion. In Ebrahimi et al. [15], the combination of a lower fitted $k_0$ and higher $M$ likely reduced local fluid drainage and increased the apparent stiffness under the indenter, improving the match with the axial reaction force, in absence of areal strain target. In addition to this, previous studies on bovine AC reported a wide range of permeability values ranging 0.0007 to 0.01 $\mathrm{mm^4\,N^{-1}\,s^{-1}}$ [82, 83]. The non-fibrillar stiffness ($E_{nf}$) was 78% lower than in Ebrahimi (Table 7.2), potentially due to both species differences and modeling choices: they fixed $\nu_{\mathrm{nf}} = 0.42$, whereas in this work $\nu_{\mathrm{nf}}$ was identified (it resulted equal to 0.46 in model 01) (Table 7.2). The value of $\nu_{\mathrm{nf}}$ likely compensated for the lower $E_{nf}$ to better capture lateral expansion. Significant differences in collagen-related parameters are also expected, as previously discussed.

A more direct comparison is possible with Julkunen et al. [14], who also tested bovine AC under unconfined compression. In their study, the average values identified for $k_0$ and $M$ were 67% higher and 33% lower, respectively, with respect to the idealized model of sample 01, while $E_{nf}$ was 71% higher (Table 7.2). Moreover, value of $\nu_{nf} = 0.22$ was not the result of an identification process; it was instead hypothesized (Table 7.2). However, Julkunen et al. [14] adopted a fibril-reinforced poroviscoelastic (FRPVE) material model, which introduces a damper in series with the non-linear spring representing the collagen network. This formulation captures the intrinsic time-dependent behavior of collagen but also increases the number of interacting parameters. Consequently, the fitted collagen-related parameters are not directly comparable. Additionally, the estimated permeability parameters can also be affected, as the presence of the damper may alter the load redistribution over time, especially during relaxation, affecting the constraining

role of collagen and the model shrinkage. As a result, the lower $M$ and higher $k_0$ obtained by Julkunen likely reflect the role of viscous damping in retaining fluid and delaying relaxation.

## 8.2. Limitations

This study explored the feasibility of non-fibrillar Poisson ratio estimation in AC using a fibril-reinforced material model. The main limitation is that mechanical and image data from only two samples were available for analysis. Despite the limited dataset, one of the two idealized models successfully captured both axial and lateral responses. The FRPE material model adopted in this work did not include the swelling behavior nor the intrinsic viscosity of collagen fibrils. However, swelling pressure was implicitly captured through the fitted non-fibrillar stiffness. Moreover, including a damping component in the collagen fibril modeling would have prevented from unique parameter identification. The orientation of collagen fibrils was idealized using the Benninghoff arcade model [84], assuming all fibrils in the superficial layer were uniformly oriented along a single direction parallel to the model surface. Although this simplification does not account for sample-specific orientations, it is widely accepted and has proven effective in reproducing key aspects of AC behavior in several samples [13, 14, 75]. Furthermore, the bovine samples originated from relatively young animals. Since the timing of the establishment of the Benninghoff collagen fibril organization during tissue maturation is still unclear [45], it is possible that the fibrillar architecture in the samples analyzed was not yet fully developed. Consequently, the collagen arrangement assumed in the model may not completely represent the structural organization of the tested tissue.

The method used to estimate the model's cross-sectional area—based on 2D convex hull projection onto the XY plane—overestimates the real area, because it neglects surface curvature and local irregularities under compression. However, in the sample-specific static configuration, where this effect was expected to be maximal, the overestimation remained within 1% when compared to the average area measured from $\mu$CT data. Regarding the experimental images, cross-sectional area was computed from segmented slices around mid-height, skipping and interpolating every 10 slices. Although this introduces simplifications, it provides a realistic representation of tissue expansion across different configurations and remains more accurate than estimates derived from optical methods alone. Other limitations include the absence of post-preload imaging, which prevented tracking early deformation stages. Finally, although the experimental protocol prescribed a nominal compressive strain of 15% of the samples' original height, microCT-based measurements revealed that the actual applied compression was approximately 13%. While the nominal value was retained in the idealized models, the measured strain was applied in the sample-specific simulations. This difference in imposed compression may have contributed to the lower total lateral expansion observed computationally for the sample-specific model. Nevertheless, given that the primary aim of this thesis was the development of a method rather than tissue intrinsic properties identification, this minor mismatch in compressive strain is not expected to significantly alter the overall conclusions.

# 9 | Conclusions

This thesis presented a novel methodology to estimate the non-fibrillar Poisson ratio of AC employing a biphasic, fiber-reinforced material model. The analysis leveraged a dataset of previously acquired synchrotron-based $\mu$CT images, including both static scans at rest and time-resolved acquisitions performed in situ during mechanical loading, which enabled dynamic tracking of areal strain. Combined with reaction forces extracted from the same unconfined compression tests, these data allowed for the simultaneous characterization of both axial and transverse macroscopic mechanical behavior. The fitting pipeline successfully reproduced both responses in the idealized model of the first sample, demonstrating the potential of the method to identify intrinsic material properties. In contrast, for the second sample the final values of the constitutive parameters did not allow to simultaneously reproduce the reaction force and lateral expansion in FE simulations, no matter if the idealized sample geometry or the sample-specific geometry was used. This behavior indicates that the difficulty originates from the sample-specific mechanical response rather than from geometric representation alone. Importantly, while previous studies reported successful fitting of sample-specific models using a single set of material parameters, those analyses relied solely on axial force data. The inclusion of the transverse response in the present framework revealed additional inter-sample variability that was more challenging to capture, suggesting that the current material model may be incapable of simultaneously reproducing both axial and transverse behaviors. These findings highlight the sensitivity of the fitting pipeline to sample-specific mechanical response and reinforce the need to investigate alternative weighting strategies and material formulations. Overall, this work provides a foundation for future analyses aimed at identifying intrinsic AC properties. Scaling this approach to larger datasets, incorporating multiple sample-specific geometries, and exploring different constitutive models will be essential to improve robustness and generalisability. Reliable estimation of intrinsic AC properties has the potential to substantially improve the predictive capacity of computational joint models, allowing simulations of OA progression and supporting the design of patient-specific implants and interventions.

# Bibliography

[1] Lynette M. March and Clarissa J.M. Bachmeier. Economics of osteoarthritis: a global perspective. *Baillière's Clinical Rheumatology*, 34(1):817–834, 1997. doi: 10.1016/S0950-5849(97)00011-8.

[2] Mika E. Mononen, Petri Tanska, Hanna Isaksson, and Rami K. Korhonen. A novel method to simulate the progression of collagen degeneration of cartilage in the knee: Data from the osteoarthritis initiative. *Scientific Reports*, 6:21415, 2016. doi: 10.1038/srep21415.

[3] S.R.Kingsbury, H.J.Gross, G.Isherwood, and et al. Osteoarthritis in europe: impact on health status, work productivity and use of pharmacotherapies in five european countries. *Rheumatology*, 53(5):937–947, 2014. doi: 10.1093/rheumatology/ket463.

[4] J. L. Whittaker, J. Runhaar, S. Bierma-Zeinstra, and E. M. Roos. A lifespan approach to osteoarthritis prevention. *Osteoarthritis and Cartilage*, 2021. doi: 10.1016/j.semarthrit.2021.11.011.

[5] David J. Hunter and Sita Bierma-Zeinstra. Osteoarthritis. *The Lancet*, 393(10182):1745–1759, 2019. doi: 10.1016/S0140-6736(19)30417-9.

[6] Steven Kurtz, Kevin Ong, Edmund Lau, Fionna Mowat, and Michael Halpern. Projections of primary and revision hip and knee arthroplasty in the united states from 2005 to 2030. *J Bone Joint Surg Am*, 89(4):780–785, 2007. doi: 10.2106/JBJS.F.00222. URL `https://pubmed.ncbi.nlm.nih.gov/17403800/`.

[7] Jasvinder A. Singh, Shaohua Yu, Lang Chen, and John D. Cleveland. Rates of total joint replacement in the united states: Future projections to 2020–2040 using the national inpatient sample. *The Journal of Rheumatology*, 46(9):1134–1140, 2019. doi: 10.3899/jrheum.170990.

[8] Yanxi Liu, Karan M. Shah, and Jian Luo. Strategies for articular cartilage repair and regeneration. *Frontiers in Bioengineering and Biotechnology*, 9:770655, 2021. doi: 10.3389/fbioe.2021.770655. URL `https://pmc.ncbi.nlm.nih.gov/articles/PMC8719005/`.

[9] Seyed Ali Elahi, Petri Tanska, Satanik Mukherjee, Rami K. Korhonen, Liesbet Geris, Ilse Jonkers, and Nele Famaey. Guide to mechanical characterization of articular cartilage and hydrogel constructs based on a systematic in silico parameter sensitivity analysis. *Journal*

*of the Mechanical Behavior of Biomedical Materials*, 124:104795, 2021. doi: 10.1016/j.jbiomech.2021.110677.

[10] Young Guk Kim, Jonghoon Choi, and Kyobum Kim. Mesenchymal stem cell-derived exosomes for effective cartilage tissue repair and treatment of osteoarthritis. *Biotechnology Journal*, 2020. doi: 10.1002/biot.202000123.

[11] Renzo Phellan, Bahe Hachem, Julien Clin, Jean-Marc Mac-Thiong, and Luc Duong. Real-time biomechanics using the finite element method and machine learning: Review and perspective. *Medical Physics*, 48(1):7–18, 2021. doi: 10.1002/mp.14602. Epub 2020Dec7.

[12] T. Rödder, J. Will, M. Siebert, J. Fehr, and J. Lang. Parameter identification for material models – how to cope with the increasing complexity? In *Proceedings of the NAFEMS World Congress*. NAFEMS, 2015.

[13] W. Wilson, C.C. van Donkelaar, B. van Rietbergen, K. Ito, and R. Huiskes. Stresses in the local collagen network of articular cartilage: a poroviscoelastic fibril-reinforced finite element study. *Journal of Biomechanics*, 37:357–366, 2004. doi: 10.1016/S0021-9290(03)00267-7.

[14] P. Julkunen, P. Kiviranta, W. Wilson, J. S. Jurvelin, and R. K. Korhonen. Characterization of articular cartilage by combining microscopic analysis with a fibril-reinforced finite-element model. *Journal of Biomechanics*, 40(8):1862–1870, 2007. doi: 10.1016/j.jbiomech.2006.11.021.

[15] Mohammadhossein Ebrahimi, Mikko A. J. Finnilä, Aleksandra Turkiewicz, Martin Englund, Simo Saarakkala, Rami K. Korhonen, and Petri Tanska. Elastic, dynamic viscoelastic and model-derived fibril-reinforced poroelastic mechanical properties of normal and osteoarthritic human femoral condyle cartilage. *Annals of Biomedical Engineering*, 49(9):2622–2634, 2021. doi: 10.1007/s10439-021-02838-4.

[16] W. M. Lai C. G. Armstrong V. C. Mow, S. C. Kuei. Biphasic creep and stress relaxation of articular cartilage in compression: Theory and experiments. *Journal of Biomechanical Engineering*, 102:73–84, 1980. doi: 10.1115/1.3138202.

[17] J. S. Jurvelin, M. D. Buschmann, and E. B. Hunziker. Optical and mechanical determination of poisson's ratio of adult bovine humeral articular cartilage. *Journal of Biomechanics*, 30(3):235–241, 1997. doi: 10.1016/S0021-9290(96)00133-9.

[18] Wassif Kabir, Claudia Di Bella, and Cathal D. O'Connell. Assessment of native human articular cartilage: A biomechanical protocol. *Cartilage*, $13(2_{s}uppl), 2020. doi : .$

Joseph M. Mansour. *Biomechanics of Cartilage*. PhD thesis, Case Western Reserve University, 2003. Kinesiology: The Mechanics and Pathomechanics of Human Movement, 2nd edition, pp. 66–79.

Elisa Belluzzi, Silvia Todros, Assunta Pozzuoli, Pietro Ruggieri, Emanuele Luigi Carniel, and Alice Berardo. Human cartilage biomechanics: Experimental and theoretical approaches towards the identification of mechanical properties in healthy and osteoarthritic conditions. *Processes*, 11, 2023. 10.3390/pr11041014.

Mengqi Guan, Qingyuan Yu, Guohui Zhou, Yan Wang, Jianan Yu, Wei Yang, and Zhenhua Li. Mechanisms of chondrocyte cell death in osteoarthritis: Implications for disease progression and treatment. *Journal of Orthopaedic Surgery and Research*, 19(1):55, 2024. 10.1186/s13018-024-05055-6.

Hector Dejea, Maria Pierantoni, Gustavo A. Orozco, E. Tobias B. Wrammerfors, Stefan J. Gstöhl, Christian M. Schlepütz, and Hanna Isaksson. In situ loading and time-resolved synchrotron-based phase contrast tomography for the mechanical investigation of connective knee tissues: A proof-of-concept study. *Advanced Science*, 11(21):2308811, 2024. 10.1002/advs.202308811.

S. D. Masouros, A. M. J. Bull, and A. A. Amis. Biomechanics of the knee joint. *Orthopaedics and Trauma*, 24:84–91, 2010. https://doi.org/10.1016/j.mporth.2010.03.005.

Darryl D. D'Lima, Benjamin J. Fregly, Shantanu Patil, Nikolai Steklov, and Clifford W. Jr Colwell. Knee joint forces: prediction, measurement, and significance. *Sage Journals*, 226: 95–102, 2012. https://doi.org/10.1177/0954411911433372.

Bhaskar Kumar Madeti, Srinivasa Rao Chalamalasetti, and S. K. Sundara Siva Rao Bolla Pragada. Biomechanics of knee joint - a review. *Frontiers of Mechanical Engineering*, 10:176–186, 2015. https://doi.org/10.1007/s11465-014-0306-x.

Alexander Paz, Gustavo A. Orozco, Rami K. Korhonen, José J. García, and Mika E. Mononen. Expediting finite element analyses for subject-specific studies of knee osteoarthritis: A literature review. *Applied Sciences*, 11(23):11440, 2021. 10.3390/app112311440.

Sofia Oliveira, Betina B. Hinckel, Filipe S. Silva, Óscar Carvalho, and Ana Leal. A guide to articular cartilage functioning: a comprehensive review, current challenges and mechanobiological solutions. *Prog Biomed Eng (Bristol)*, 7(3), 2025. 10.1088/2516-1091/ade83a.

Joerg Eschweiler, Nils Horn, Bjoern Rath, Marcel Betsch, Alice Baroncini, Markus Tingart, and Filippo Migliorini. The biomechanics of cartilage—an overview. *Life*, 11(4):302, 2021. 10.3390/life11040302.

Enzo S. Mameri, Suhas P. Dasari, Luc M. Fortier, Fernando Gómez Verdejo, Safa Gursoy, Adam B. Yanke, and Jorge Chahla. Review of meniscus anatomy and biomechanics. *Current Reviews in Musculoskeletal Medicine*, 15:323–335, 2022. https://doi.org/10.1007/s12178-022-09768-1.

Peter S. Walker, Sally Arno, Christopher Bell, Gaia Salvadore, Ilya Borukhov, and Cheongeun Oh. Chapter 2 - histology and biomechanics of knee joint. *Journal of Biomechanics*, 48: 1383–1388, 2015. https://doi.org/10.1016/j.jbiomech.2015.02.055.

Hazari Animesh. *Cartilage Tissue and Knee Joint Biomechanics*. 2024.

Li Zhang, Geng Liu, Bing Han, Zhe Wang, Yuzhou Yan, Jianbing Ma, and Pingping Wei. Knee joint biomechanics in physiological conditions and how pathologies can affect it: A systematic review. *Applied Bionics and Biomechanics*, 2020. https://doi.org/10.1155/2020/7451683.

Aiyong Cui, Huizi Li, Dawei Wang, Junlong Zhong, Yufeng Chen, and Huading Lu. Global, regional prevalence, incidence and risk factors of knee osteoarthritis in population-based studies. *eClinicalMedicine*, 29:100587, 2020. 10.1016/j.eclinm.2020.100587.

Prakash Shah, Amol Patil, Ali Zaidi, et al. Variation in the thickness of knee cartilage. the use of a novel method for mri analysis. *The Journal of Arthroplasty*, 34(8):1841–1846.e1, 2019. 10.1016/j.arth.2019.05.006.

Laura Weimer, Luisa M. Schmidt, Gerhard Sengle, Marcus Krüger, Alan M. Smith, Ilona Brändlin, and Frank Zaucke. Localisation-dependent variations in articular cartilage ecm: Implications for tissue engineering and cartilage repair. *International Journal of Molecular Sciences*, 26(19):9331, 2025. 10.3390/ijms26199331.

Hemanth Akkiraju and Anja Nohe. Role of chondrocytes in cartilage formation, progression of osteoarthritis and cartilage regeneration. *Journal of Developmental Biology*, 3(4):177–192, 2015. 10.3390/jdb3040177. URL `https://www.mdpi.com/2221-3759/3/4/177`.

Robert L. Trevi no, Carol A. Pacione, AnneMarie Malfait, Susan Chubinskaya, and Markus A. Wimmer. Development of a cartilage shear-damage model to investigate the impact of surface injury on chondrocytes and extracellular matrix wear. *Cartilage*, 8(4):444–455, 2017. 10.1177/1947603516681133.

A.R. Gannon, T.Nagel, and D.J. Kelly. The role of the superficial region in determining the dynamic properties of articular cartilage. *Osteoarthritis and Cartilage*, 20(11):1417–1425, 2012. 10.1016/j.joca.2012.08.005.

Mohammadhossein Ebrahimi. *Structure, Composition and Function of Human Tibiofemoral Joint Cartilage – Experimental and Computational Analysis of Healthy and Osteoarthritic Tissue*. PhD thesis, University of Eastern Finland, Department of Applied Physics, Kuopio, 2022.

M. Rauwolf, A. Turyanskaya, P. Wobrauschek, K. Sawhney, A. Roschger, P. Roschger, C. Streli, and J. G. Hofstaetter. Thickness determination of the tidemark of human articular cartilage using high-resolution micro-xrf imaging of zinc and lead. *Osteoarthritis and Cartilage Open*, 3, 2021. 10.1016/j.ocarto.2021.100182.

C. S. Black, P. K. Crepeau, I. D. Sheffield, J. R. Macdonald, D. J. Wootton, M. Baek, D. L. Eggett, P. R. Reynolds, and D. L. Kooyman. Identification of the tidemark line of calcification in osteoarthritic cartilage using a stain for alkaline phosphatase. *Osteoarthritis and Cartilage*, 23, 2015. 10.1016/j.joca.2015.02.876.

Sylvie Ricard-Blum. The collagen family. *Cold Spring Harbor Perspectives in Biology*, 3(1): a004978, 2011. 10.1101/cshperspect.a004978.

Yunyun Luo, Dovile Sinkeviciute, Yi He, Morten Karsdal, Yves Henrotin, Ali Mobasheri, Patrik Önnerfjord, and Anne Bay-Jensen. The minor collagens in articular cartilage. *Protein & Cell*, 8:560–572, 2017. 10.1007/s13238-017-0377-7.

Adam Maria Gadomski, Natalia Kruszewska, Ivan Santamaría-Holek, J. J. Uher, Z. Pawlak, A. Oloyede, E. Pechkova, and C. Nicolini. Can modern statistical mechanics unravel some practical problems encountered in model biomatter aggregations emerging in internal- and external-friction conditions? In Byung-Soo Kim, editor, *Statistical Mechanics Research*, pages 44–98. Nova Science Publishers, New York, 2008. ISBN 978-1-60456-029-9.

Jet R. Peters, Marit Hoogenboom, Florencia Abinzano, Sebastien J.P. Callens, Jasper Foolen, and Keita Ito. Tissue growth as a mechanism for collagen fiber alignment in articular cartilage. *Nature*, 2024. 10.1038/s41598-024-82441-4.

Anna A. Cederlund and Richard M. Aspden. Walking on water: revisiting the role of water in articular cartilage biomechanics in relation to tissue engineering and regenerative medicine. *Bioengineering*, 9(8):347, 2022. 10.3390/bioengineering9080347.

Robert Karpiński, Aleksandra Prus, Jacek Baj, Sebastian Radej, Marcin Prządka, Przemysław Krakowski, and Kamil Jonak. Articular cartilage: Structure, biomechanics, and the potential of conventional and advanced diagnostics. *Applied Sciences*, 15(12):6896, 2025. 10.3390/app15126896.

Lourdes Alcaide-Ruggiero, Ramón Cugat, and Juan Manuel Domínguez. Proteoglycans in articular cartilage and their contribution to chondral injury and repair mechanisms. *International Journal of Molecular Sciences*, 24, 2023. 10.3390/ijms241310824.

J. Casale and Jonathan S. Crane. Glycosaminoglycans, 2023.

Gerard A. Ateshian. The role of interstitial fluid pressurization in articular cartilage lubrication. *Journal of Biomechanics*, 42(9):1163–1176, 2009. 10.1016/j.jbiomech.2009.04.040.

M.Favero, R.Ramonda, M.B.Goldring, S.R.Goldring, and L.Punzi. Early knee osteoarthritis. *RMD Open*, 1(suppl 1):e000062, 2015. 10.1136/rmdopen-2015-000062.

Seonghun Park, Ramaswamy Krishnan, Steven B. Nicoll, and Gerard A. Ateshian. Cartilage interstitial fluid load support in unconfined compression. *Journal of Biomechanics*, 36(12): 1785–1796, 2003. https://doi.org/10.1016/S0021-9290(03)00231-8.

G. A. Ateshian, W. H. Warden, J. J. Kim, R. P. Grelsamer, and V. C. Mow. Finite deformation biphasic material properties of bovine articular cartilage from confined compression experiments. *Journal of Biomechanics*, 30(11-12):1157–1164, 1997. 10.1016/S0021-9290(97)85606-0.

Weijian Lin, Qingen Meng, Junyan Li, Zhenxian Chen, and Zhongmin Jin. The effect of highly inhomogeneous biphasic properties on mechanical behaviour of articular cartilage. *Computer*

*Methods and Programs in Biomedicine*, 208:106122, 2021. 10.1016/j.cmpb.2021.106122.

P. Kiviranta et al. Collagen network primarily controls poisson's ratio of bovine articular cartilage in compression. *Journal of Orthopaedic Research*, 24(4):690–699, 2006. 10.1002/jor.20107.

Van C. Mow and X. Edward Guo. Mechano-electrochemical properties of articular cartilage: their inhomogeneities and anisotropies. *Annual Review of Biomedical Engineering*, 4:175–209, 2002. 10.1146/annurev.bioeng.4.110701.120309.

Mathieu Charlebois, Marc D. McKee, and Michael D. Buschmann.

Rami K. Korhonen and Jukka S. Jurvelin. Compressive and tensile properties of articular cartilage in axial loading are modulated differently by osmotic environment. *Medical Engineering & Physics*, 32(2):155–160, 2010. 10.1016/j.medengphy.2009.11.004.

Syeda Atiqa Batool, Bradley J. Roth, and Yang Xia. Depth-dependent strain model (1d) for anisotropic fibrils in articular cartilage. *Materials*, 17(1):238, 2024. 10.3390/ma17010238.

Angelo Morro. Modelling of viscoelastic materials and creep behaviour. *AAPP | Atti della Accademia Peloritana dei Pericolanti. Classe di Scienze Fisiche, Matematiche e Naturali*, 94 (2):A3, 2016. 10.1478/AAPP.942A3.

Dongze Wang, Gregory de Boer, Anne Neville, and Ali Ghanbarzadeh. A review on modelling of viscoelastic contact problems. *Lubricants*, 10(12):358, 2022. 10.3390/lubricants10120358.

Allison Okamura Sarthak Misra, K.T. Ramesh. Modeling of tool-tissue interactions for computer-based surgical simulation: A literature review. *Presence: Teleoperators and Virtual Environments*, 17, 2008. 10.1162/pres.17.5.463.

Ivan Argatov. Mathematical modeling of linear viscoelastic impact: Application to drop impact testing of articular cartilage. *Tribology International*, 63:213–225, 2013. 10.1016/j.triboint.2012.09.014.

Pedro J. Caballero and Néstor Arzola. Revisión de modelos constitutivos para cartílago articular. *Revista Mexicana de Ingeniería Biomédica*, 33(1):41–52, 2012.

Wouter Wilson, Corrinus C van Donkelaar, Bert van Rietbergen, and Rik Huiskes. A fibril-reinforced poroviscoelastic swelling model for articular cartilage. *Journal of Biomechanics*, 38 (6):1195–1204, 2005. 10.1016/j.jbiomech.2004.06.017.

Rami K. Korhonen, Mikko S. Laasanen, Juha Töyräs, Reijo Lappalainen, Heikki J. Helminen, and Jukka S. Jurvelin. Fibril reinforced poroelastic model predicts specifically mechanical behavior of normal, proteoglycan depleted and collagen degraded articular cartilage. *Journal of Biomechanics*, 36(9):1373–1379, 2003. 10.1016/S0021-9290(03)00069-1.

Umair Farooq and J. I. Siddique. Compressive stress relaxation behavior of articular cartilage and its effects on fluid pressure and solid displacement due to non-newtonian flow. *Computer Methods in Biomechanics and Biomedical Engineering*, 24(2):161–172, 2021. 10.1080/10255842.2020.1817408

L. Vikingsson, J. A. Gómez-Tejedor, G. Gallego Ferrer, and J. L. Gómez Ribelles. An experimental fatigue study of a porous scaffold for the regeneration of articular cartilage. *Journal of Biomechanics*, 48(7):1310–1317, 2015. 10.1016/j.jbiomech.2015.02.013.

W. M. Lai, J. S. Hou, and V. C. Mow. A triphasic theory for the swelling and deformation behaviors of articular cartilage. *Journal of Biomechanical Engineering*, 113(3):245–258, 1991. 10.1115/1.2894880.

L. P. Li, M. D. Buschmann, A. Shirazi-Adl, and A. J. Grodzinsky. A fibril reinforced nonhomogeneous poroelastic model for articular cartilage. *Journal of Biomechanics*, 33(12):1563–1573, 2000. 10.1016/S0021-9290(00)00153-6.

Lihai Zhang, Saeed Miramini, David W. Smith, Bruce S. Gardiner, and Alan J. Grodzinsky. Time evolution of deformation in a human cartilage under cyclic loading. *Annals of Biomedical Engineering*, 43(5):1166–1177, 2015. 10.1007/s10439-014-1164-8.

Lassi Rieppo, Jarno Rieppo, S. Jurvelin, Jukka and Simo Saarakkala. Fourier transform infrared spectroscopic imaging and multivariate regression for prediction of proteoglycan content of articular cartilage. *PLoS ONE*, 7(2):e32344, 2012. 10.1371/journal.pone.0032344. URL `https://doi.org/10.1371/journal.pone.0032344`.

W. Wilson, J.M. Huyghe, and C.C. van Donkelaar. Depth-dependent compressive equilibrium properties of articular cartilage explained by its composition. *Biomechanics and Modeling in Mechanobiology*, 6(1-2):43–53, 2007. 10.1007/s10237-006-0044-z. URL `https://doi.org/10.1007/s10237-006-0044-z`.

K. S. Halonen, M. E. Mononen, J. S. Jurvelin, J. Töyräs, and R. K. Korhonen. Importance of material properties and structural representations in 3d computational modeling of articular cartilage. *Journal of Biomechanics*, 46(6):1184–1192, 2013. 10.1016/j.jbiomech.2013.01.017.

Viktor Jönsson, Gustavo A. Orozco, Maria Pierantoni, Hector Dejea, Anna Gustafsson, Lorenzo Grassi, and Hanna Isaksson. Influence of articular cartilage sample geometry on mechanical response and properties using finite element simulation. *Journal of Biomechanics*, 176, 2024. 10.1016/j.jbiomech.2024.112323.

Caroline A. Schneider, Wayne S. Rasband, and Kevin W. Eliceiri. Nih image to imagej: 25 years of image analysis. *Nature Methods*, 9(7):671–675, 2012. 10.1038/nmeth.2089.

Marco A. Luersen and Rodolphe Le Riche. Globalized nelder–mead method for engineering optimization. *Computers Structures*, 82(23-26):2251–2260, 2004. 10.1016/j.compstruc.2004.03.072.

Andriy Fedorov, Reinhard Beichel, Jayashree Kalpathy-Cramer, Julien Finet, Jean-Christophe Fillion-Robin, Sonia Pujol, Christian Bauer, Dominique Jennings, Fiona Fennessy, Milan Sonka, John Buatti, Stephen Aylward, James V. Miller, Steve Pieper, and Ron Kikinis. 3d slicer as an image computing platform for the quantitative imaging network. *Magnetic Resonance Imaging*, 30(9):1323–1341, 2012. 10.1016/j.mri.2012.05.001.

CIBC Seg3D. Volumetric image segmentation and visualization. *Scientific Computing and Imaging Institute (SCI)*, 2016.

Philip E. Riches. Sensitivity analysis of permeability parameters of bovine nucleus pulposus obtained through inverse fitting of the nonlinear biphasic equation: effect of sampling strategy. *Computer Methods in Biomechanics and Biomedical Engineering*, 14(1):29–36, 2011. 10.1080/10255842.2010.544301.

Duncan K. Temple, Anna A. Cederlund, Bernard M. Lawless, Richard M. Aspden, and Daniel M. Espino. Viscoelastic properties of human and bovine articular cartilage: a comparison of frequency-dependent trends. *BMC Musculoskeletal Disorders*, 17(1):419, 2016. 10.1186/s12891-016-1279-1.

L.P. Li, R.K. Korhonen, J. Iivarinen, J.S. Jurvelin, and W. Herzog. Fluid pressure driven fibril reinforcement in creep and relaxation tests of articular cartilage. *Medical Engineering & Physics*, 30(2):182–189, 2008. 10.1016/j.medengphy.2007.03.001.

P. Julkunen, R. K. Korhonen, W. Herzog, and J. S. Jurvelin. Mechanical characterization of articular cartilage by combining magnetic resonance imaging and finite-element analysis—a potential functional imaging technique. *Medical Engineering & Physics*, 30(4):506–515, 2008. 10.1016/j.medengphy.2007.05.012.

A. Benninghoff. Form und bau der gelenkknorpel in ihren beziehungen zur funktion: Zweiter teil: Der aufbau des gelenkknorpels in seinen beziehungen zur funktion. *Zeitschrift für Zellforschung*, 2:783–862, 1925. 10.1007/BF00583443.

# A | List of Figures

Figure 2.1: Schematic of the knee joint anatomy, frontal (left) and coronal (right) views [26]. . . . . 8

Figure 3.1: AC layers: superficial, middle, deep, and calcified zone. The image illustrates collagen fibril orientation, chondrocyte morphology, and the tidemark. Adapted from [28]. . . . . 11

Figure 3.2: Structure of a PG aggregate: multiple aggrecan molecules bind to a central hyaluronan filament via link proteins, forming a large supramolecular complex. Adapted from [48]. . . . . 13

Figure 4.1: Typical mechanical responses of viscoelastic materials in a creep test and in stress-relaxation test. (A) Creep test: under the application of a constant stress, the strain shows an immediate elastic component followed by a gradual viscoelastic deformation; when the load is removed, an elastic followed by a viscoelastic recovery can be observed. (B) Stress-relaxation test: under constant strain, the initial stress decreases over time until it reaches a plateau. Adapted from [62]. . . . . 16

Figure 4.2: Classical mechanical models used to describe the behavior of viscoelastic materials. Maxwell model (A), Kelvin-Voigt model (B), Zener model (C) [62]. . 17

Figure 4.3: Comparative schematic of three experimental setups used to apply mechanical loading to articular cartilage - confined compression test (A), unconfined compression test (B), indentation test (C). Image taken from [27]. . . . . 19

Figure 5.1: Schematic representation of a single primary collagen fibril bundle and its depth-dependent orientations according to Benninghoff arcade model. Adapted from [13]. . . . . 21

Figure 5.2: Schematic representation of the random orientation of secondary collagen fibrils. Adapted from [13]. . . . . 22

Figure 5.3: Schematic representation of the mechanical behavior of a collagen fibril. . . . 22

Figure 6.1: Overview of the main steps of the thesis workflow. . . . . 26

Figure 6.2: Schematic of the stress-relaxation protocol used for AC samples testing. Green crosses indicate static scans, while red bars represent dynamic scans. Adapted from [22]. . . . . 27
Figure 6.3: Orthogonal static views (XY, XZ, YZ planes) of sample 01 and 02. Two enlarged insets are provided to improve the visualization of chondrocytes. . . 29
Figure 6.4: XZ orthogonal dynamic views showing the response of sample 02 after 15% and 30% compression. . . . . 30
Figure 6.5: Schematic representation of the main irregularities observed in bovine AC samples. Data shown refers to the 7th dynamic scan of sample 04 (see Table 6.1). Similar irregularities have been observed in previous studies [75]. . . 30
Figure 6.6: Example of manual segmentation in ImageJ for a slice of sample 02. The white dots represent the polygon vertices selected to delineate the tissue boundary during segmentation. . . . . 31
Figure 6.7: Idealized FE model of AC showing boundary conditions for displacement-controlled load on the top surface, constrains at the bottom surface, and free fluid flow through the lateral surfaces. . . . . 33
Figure 6.8: Schematic representation of $ConvexHull$ algorithm. Given a set of points, the convex hull is defined as the smallest convex polygon that contains all the points. . . . . 35
Figure 6.9: Fitting workflow corresponding to a single restart of the GBNM-based routine. A new initial guess is automatically generated after convergence, resulting in a continuous loop. . . . . 36
Figure 6.10: Experimental reaction force-time curve (red line). The yellow markers indicate the selected experimental data time points used for the fitting procedure and computation of the objective function. . . . . 37
Figure 6.11: Overview of the sample-specific model and fitting procedure. A) The sample-specific model (ID 02). B) XZ view showing the nodes selection process. C) XY view describing the area calculation method. D) Example of lateral expansion fitting, where cumulative strains are illustrated. E) Example of reaction force fitting. . . . . 38

Figure 7.1: Results of the optimization for the idealized models of samples 01 and 02. A-B) Sample 01: simulated reaction forces fitted to the experimental stress-relaxation response (A) and lateral expansion fitting based on the areal strain computed between the undeformed configuration (1st static scan) and the deformed states after the first and second loading ramps (7th dynamic and 2nd static scans) (B). C-D) Sample 02: fitting results for reaction force (C) and lateral expansion (D), evaluated using the same deformation states as in sample 01. Quantitative deviations are summarized in Table 7.3. . . . . 40

Figure 7.2: The axial logarithmic strain distribution is illustrated for both the sample-specific (A) and idealized (B) model of sample 02. . . . . 41
Figure 7.3: Results of the optimization for the sample-specific model of sample 02. A) Simulated reaction forces fitted to the experimental stress-relaxation response. B) Lateral expansion fitting based on the areal strain computed between the undeformed configuration (1st static scan) and the deformed states after the first and second loading ramps (7th dynamic and 2nd static scans). Quantitative deviations are summarized in Table 7.3. . . . . 42

# B | List of Tables

Table 3.1: General composition of AC expressed as percentage of total wet weight [28]. . 10

Table 6.1: Summary of the available specimens tested in stress-relaxation experiment [22], with related observations and assessment for their suitability for the analysis. 28

Table 6.2: Material model parameters and optimization ranges [9, 13, 14, 75]. In line with previous studies [13, 14], the parameter $C$ value was fixed. . . . . 34

Table 7.1: Lateral expansion values (%) obtained measuring the $\mu$CT images for the two selected samples (more details in Section 6.2). . . . . 39

Table 7.2: Fitted FRPE material parameters for both idealized and sample-specific models. Literature data from [14, 15] are included for comparison. Values marked with * were fixed during the optimization. Note that Julkunen et al. employed a fibril-reinforced poroviscoelastic (FRPVE) material model. . . . . 43

Table 7.3: Relative differences (%) between the experimental and computational data for both reaction forces and areal strains at selected time points. . . . . 43

# Acknowledgements

I would like to thank Viktor Jönsson, who supervised and trained me throughout the entire project. The many stimulating discussions we had and his active contribution to the analyses and discoveries were fundamental to the development of this work. Beyond the scientific guidance, I am truly grateful for his human support and encouragement, especially during the most challenging moments of the project, which made this experience not only formative, but genuinely enriching.

I would also like to sincerely thank my thesis advisor at Lund University, Professor Hanna Isaksson, who gave me the opportunity to boost my interests in the field of computational biomechanics by proposing this thesis project and welcoming me into the Biomechanics group, a stimulating, international, and innovative research environment at the Biomedical Centre (BMC) in Lund. I am deeply grateful for the experience I lived and for the personal and scientific growth it brought me.

Finally, I would like to thank my thesis advisor at Politecnico di Milano, Professor Emiliano Votta, for giving me the opportunity to live such a formative and life-changing experience, and for his constant willingness to be there whenever needed, always with kindness and trust, even from a distance.

*Marco Sartorio*